The Role of Horizontal Temperature Advection in Arctic Amplification

JOSEPH P. CLARK,[a] VIVEK SHENOY,[a,b] STEVEN B. FELDSTEIN,[a] SUKYOUNG LEE,[a] AND MICHAEL GOSS[a,c]

[a] *Department of Meteorology and Atmospheric Science, The Pennsylvania State University, University Park, Pennsylvania*
[b] *School of Meteorology, University of Oklahoma, Norman, Oklahoma*
[c] *Department of Earth System Science, Stanford University, Stanford, California*

(Manuscript received 17 December 2019, in final form 24 December 2020)

ABSTRACT: The wintertime (December–February) 1990–2016 Arctic surface air temperature (SAT) trend is examined using self-organizing maps (SOMs). The high-dimensional SAT dataset is reduced into nine representative SOM patterns, with each pattern exhibiting a decorrelation time scale of about 10 days and having about 85% of its variance coming from intraseasonal time scales. The trend in the frequency of occurrence of each SOM pattern is used to estimate the interdecadal Arctic winter warming trend associated with the SOM patterns. It is found that trends in the SOM patterns explain about one-half of the SAT trend in the Barents and Kara Seas, one-third of the SAT trend around Baffin Bay, and two-thirds of the SAT trend in the Chukchi Sea. A composite calculation of each term in the thermodynamic energy equation for each SOM pattern shows that the SAT anomalies grow primarily through the advection of the climatological temperature by the anomalous wind. This implies that a substantial fraction of Arctic amplification is due to horizontal temperature advection that is driven by changes in the atmospheric circulation. An analysis of the surface energy budget indicates that the skin temperature anomalies as well as the trend, although very similar to that of the SAT, are produced primarily by downward longwave radiation.

KEYWORDS: Arctic; Teleconnections; Climate change; Thermodynamics; Interdecadal variability; Trends

1. Introduction

Over the Arctic, the surface air temperature (SAT; the temperature at a height of approximately 2 m above Earth's surface) has increased by twice that of the global average (Chylek et al. 2009; Bekryaev et al. 2010), with the amplitude of this warming being largest during winter (Serreze and Francis 2006). This phenomenon is known as Arctic amplification. The impacts of this rapid Arctic SAT increase, associated rapid sea ice loss (e.g., Francis and Hunter 2006), and subsequent societal and ecological implications have prompted studies into the underlying cause.

Processes implicated as potential drivers of Arctic amplification include surface-based feedbacks involving sea ice loss (e.g., Budyko 1969; Sellers 1969; Serreze et al. 2009; Screen and Simmonds 2010), changes in oceanic heat transport (e.g., Chylek et al. 2009), changes in atmospheric heat transport (e.g., Graversen 2006; Graversen et al. 2008; Hwang and Frierson 2010; Lee et al. 2011; Woods et al. 2013; Ding et al. 2014; Woods and Caballero 2016; Gong et al. 2017; Lee et al. 2017; Armour et al. 2019), changes in cloud radiative forcing (e.g., Francis and Hunter 2007), and increases in anthropogenic soot (e.g., Quinn et al. 2008).

The sea ice albedo feedback mechanism is hypothesized to operate over the Arctic during both summer and winter, due to the following chain of events: Summertime sea ice loss, which is amplified by the sea ice albedo feedback mechanism, exposes the ocean's surface, resulting in an upward flux of heat into the lower troposphere during the subsequent winter (e.g., Deser et al. 2010). The chain of events that links summertime sea ice loss to wintertime Arctic warming in the lower troposphere has been argued to be supported by observations, which show that the Arctic temperature trend is most pronounced in the lower troposphere (Serreze et al. 2009; Screen and Simmonds 2010; Screen et al. 2012; Walsh 2014; Dai et al. 2019). However, there are other plausible mechanisms that can also explain why the wintertime Arctic warming trend is most pronounced in the lower troposphere. For example, a bottom-heavy Arctic warming pattern can also be seen in response to forcing by the tropical Madden–Julian oscillation (MJO; Yoo et al. 2013), whereby convection associated with the MJO excites poleward-propagating Rossby waves that transport warm moist air into the Arctic. Woods and Caballero (2016) and Baggett et al. (2016) showed that when warm moist air intrudes into the Arctic, the greatest temperature increase occurs near the surface because the warm-air advection effectively erodes the temperature inversion. The results of those studies bring into question the notion that a bottom-heavy Arctic winter warming trend is evidence for the driving by local diabatic processes, such as upward surface sensible and latent heat fluxes associated with sea ice loss.

Previous studies showed that intraseasonal teleconnection patterns, such as those driven by the MJO, can have an important influence on fluctuations at much longer time scales, such as Arctic amplification (Yoo et al. 2013). For example, when multiple intraseasonal teleconnection events of the same phase occur within a single season, the time-mean climate for that season is altered. Interdecadal climate trends can then be altered by a trend in the frequency of occurrence of intraseasonal teleconnection patterns. An example of this relationship has been shown for the interdecadal trend of the zonal-mean zonal wind, for which most of the interdecadal variability can be explained by the interdecadal trend in the

Supplemental information related to this paper is available at the Journals Online website: https://doi.org/10.1175/JCLI-D-19-0937.s1.

Corresponding author: Joseph Clark, juc414@psu.edu

DOI: 10.1175/JCLI-D-19-0937.1

frequency of intraseasonal teleconnections (Lee and Feldstein 2013; Feldstein and Lee 2014).

The primary aim of this study is to determine the fraction of the Arctic warming trend that can be accounted for by changes in the frequency of occurrence of atmospheric spatial patterns that are dominated by their intraseasonal-time-scale contribution. Although it is certainly to be expected that some fraction of the Arctic warming trend arises from interannual processes, for our study we examine only the impact of intraseasonal-time-scale processes. Intraseasonal processes are usually understood to arise from natural variability; however, the results presented in this study should not automatically be considered as arising from natural variability because intraseasonal processes may also be influenced by external forcings, such as increasing CO_2 concentrations. For example, Compo and Sardeshmukh (2009) showed that increased sea surface temperatures, due to increased CO_2 concentrations, can excite intraseasonal-time-scale Rossby waves. In this study, we do not investigate whether the intraseasonal contribution to Arctic amplification is due to natural variability or is a forced response to increased greenhouse gas concentrations.

To investigate the physical processes that drive the SAT changes associated with Arctic amplification, we will use the thermodynamic energy equation, since the level of the SAT is close to but not precisely at the surface. Many other studies that examine SAT changes over the Arctic use the surface energy budget (instead of the thermodynamic energy equation), which is derived by applying the first law of thermodynamics to Earth's surface, which is often a solid (except when the surface is water). The temperature at Earth's surface is typically referred to as the skin temperature (SKT). However, away from the surface, including at a height of 2 m (i.e., the height corresponding to the SAT), it is necessary to examine Arctic amplification using the thermodynamic energy equation, which applies to fluids. Although both the surface energy budget and the thermodynamic energy equation are derived from the first law of thermodynamics, the advection terms in the thermodynamic energy equation vanish over solid surfaces because the horizontal and vertical velocity approach zero at the surface. This leads to different governing equations for temperatures that are separated by only 2 m. In this study, we examine both temperatures (the SKT and SAT) and discuss why the differences between them are important, and perhaps underappreciated in the context of Arctic amplification.

The thermodynamic energy equation, which applies to the SAT, can be written as

$$\frac{\partial T}{\partial t} = -u\frac{\partial T}{\partial x} - v\frac{\partial T}{\partial y} - \dot{\eta}\frac{\partial T}{\partial \eta} + \frac{\kappa T\omega}{p} + Q_1 + Q_2 + Q_3 + Q_4. \quad (1)$$

(The equation that governs SKT changes is discussed in section 3b.) The thermodynamic energy equation indicates that temperature changes occur in response to horizontal temperature advection ($-u\partial T/\partial x - v\partial T/\partial y$), vertical temperature advection ($-\dot{\eta}\partial T/\partial \eta$), and adiabatic warming ($\kappa T\omega/p$), where η denotes the hybrid sigma–pressure vertical coordinate [the vertical coordinate in the European Centre for Medium-Range Weather Forecasts (ECMWF) reanalysis], p denotes pressure, $\dot{\eta} \equiv d\eta/dt$, $\omega \equiv dp/dt$, and κ is the ratio between the specific heat capacity of air and the dry-air gas constant (ECMWF 2014). The diabatic heating terms Q_1, Q_2, Q_3, and Q_4 correspond to longwave radiative heating/cooling, shortwave radiative heating/cooling, heating associated with turbulent eddy mixing, and latent heat release, respectively. Although turbulent eddy mixing is not truly a diabatic process, as it represents subgrid-scale vertical advection; this process is parameterized by the ECMWF reanalysis model (our data source; see section 2), which is why we include it as Q_3 in (1). The first three of the Q terms in (1) can be expressed as the three-dimensional convergence of the longwave radiative flux, shortwave radiative flux, and turbulence eddy heat flux, respectively.

Examination of (1) indicates that the Arctic SAT trend must be driven by some combination of terms on the right-hand side (rhs) of the thermodynamic energy equation. As discussed above, the upward surface sensible and latent heat fluxes associated with sea ice loss have been hypothesized to contribute to an increase in SAT. If these fluxes are to contribute to increases in SAT, their impact must be manifested in the vertical convergence of the turbulent eddy sensible and latent heat fluxes, a process that is contained in the turbulent eddy mixing term Q_3 on the rhs of (1). In spite of the fact that Arctic amplification must be driven by some combination of terms on the rhs of (1), seemingly few studies on the topic of Arctic amplification analyze the thermodynamic energy equation with observational data, opting instead to either examine the surface energy budget (e.g., Lu and Cai 2009; Lesins et al. 2012; Gong et al. 2017; Lee et al. 2017), as mentioned above, or to utilize climate model calculations (e.g., Deser et al. 2010; Dai et al. 2019). Therefore, in this study, we take a different approach by rigorously analyzing not only the surface energy budget, but also each term in the thermodynamic energy equation at the level of the SAT with observational data, with the aim to determine which terms are contributing most importantly to Arctic amplification.

This study is organized as follows. Section 2 describes the data and methods, including a discussion of self-organizing map (SOM) analysis and the thermodynamic energy equation. Section 3 documents the results of the SOM analysis, thermodynamic energy budget analysis, and surface energy budget analysis. Finally, a summary of the main findings of the study is provided in section 4.

2. Data and methods

The Arctic SAT trend is examined using the daily ECMWF interim reanalysis data (ERA-Interim; Dee et al. 2011) with a focus on the winter [December to February (DJF)] seasons beginning in 1990 and ending in 2016, a time period chosen in large part because the Arctic SAT trend has accelerated in recent decades (e.g., Gong et al. 2017; Clark and Lee 2019). The domain is chosen to be poleward of 60°N. It is important that daily data are used because the time scale of most extratropical teleconnections is about 2 weeks (Feldstein 2000). A 2.5° horizontal grid spacing is utilized for all variables.

a. *Self-organizing maps*

To understand what is driving the Arctic SAT trend over the 1990–2016 time period, the high-dimensional SAT dataset is reduced to a smaller number of representative patterns (Fig. 1)

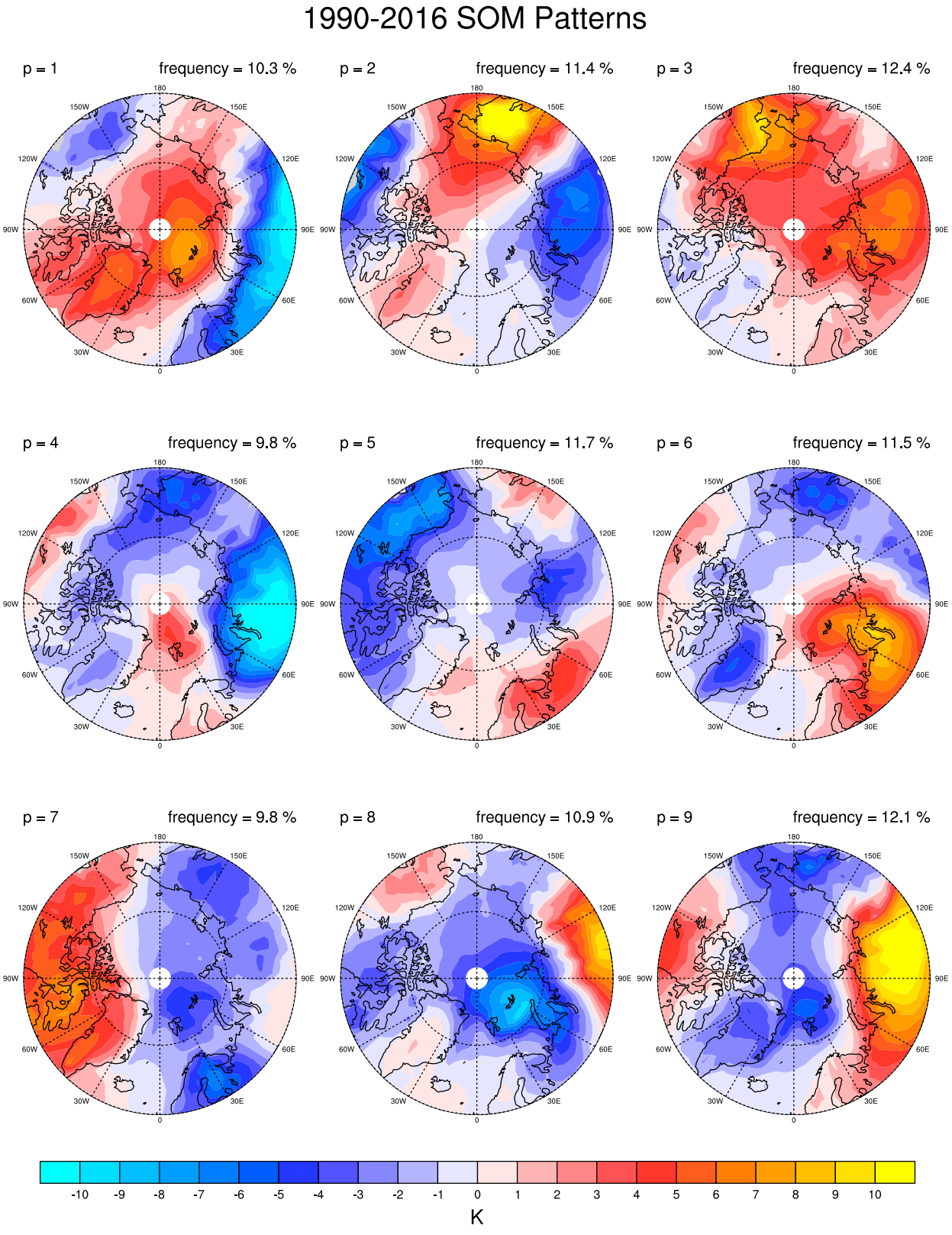

FIG. 1. Surface (2 m) air temperature anomaly patterns identified by SOM analysis using daily data from 1990 to 2016 during December–February. The value of p indicates the SOM pattern number. The frequency of occurrence of each SOM pattern is indicated above in each panel.

using SOM analysis (e.g., Kohonen 2001). SOM analysis is a clustering method that can identify patterns that recur in large datasets (e.g., Hewitson and Crane 2002; Johnson et al. 2008; Johnson and Feldstein 2010), similar to empirical orthogonal function (EOF) analysis (e.g., Kutzbach 1967). However, because the patterns identified by SOM analysis are not constrained to be orthogonal, as well as the property that SOM patterns arise from a minimization of the Euclidean distance with the observed fields, the patterns identified by SOM analysis are more likely to resemble the observed data than are EOF patterns (Yuan et al. 2015). Previous studies, such as that of Yuan et al. (2015), describe in detail the advantages of SOM analysis; therefore, we refrain from providing a more detailed discussion of SOM analysis below.

In this study, we have chosen to use a SOM grid size of 3×3, as shown in Fig. 1. The SOM analysis is applied after the SAT anomaly fields are area weighted. To determine whether the results of this study are sensitive to the size of the SOM grid, the SOM analysis was repeated for SOM grids of comparable size. For example, SOM grid sizes of 4×5, 4×4, and 9×1 had similar results to those presented in this study. The number of SOM patterns we use is based upon having enough SOM patterns to accurately represent the daily fields, but not too many SOM patterns, to ensure that the same circulation pattern is not represented more than once. A detailed discussion of this perspective can be found in Johnson et al. (2008). The sensitivity of our results for different time periods (e.g., 1979 to 2016) and domains (e.g., poleward of 50°N) was also tested, finding that the results are not sensitive to either the period or the domain size.

Our aim is to determine how the resulting cluster patterns (Fig. 1) have contributed to Arctic amplification. This is accomplished by following a methodology that has been applied in previous studies to estimate the contribution to interdecadal trends by trends in the frequency of occurrence of intraseasonal SOM patterns of the same variable (as will be shown below, the variance of the SAT SOM patterns in this study are dominated by their intraseasonal contribution) (e.g., Johnson et al. 2008; Lee and Feldstein 2013; Feldstein and Lee 2014). First, each particular DJF day is assigned a best-matching SOM pattern, defined as the SOM pattern with the smallest Euclidean distance to the SAT anomaly field on that day. This leads to a binary time series $\delta_{p,k,i}$ for each SOM pattern p, where i is the day and k the DJF season, with i having 90 values (or 91 values on leap years) for each of the 26 DJF seasons. This binary time series $\delta_{p,k,i}$ is equal to 1.0 on days when SOM pattern p is the best-matching pattern, and zero otherwise. The DJF-mean SAT anomaly, for each DJF season, can then be approximated as a linear combination of the nine SOM patterns, where each SOM pattern is weighted by its frequency of occurrence, $f_{p,k}$, within each DJF season; that is,

$$\widehat{\mathrm{SAT}}(x,y)_k \approx \sum_{p=1}^{N\mathrm{pats}} \sum_{k=1}^{26} \sum_{i=1}^{N\mathrm{days}} \frac{\delta_{p,k,i}}{N\mathrm{days}} \mathrm{SAT}_p(x,y) = \sum_{p=1}^{N\mathrm{pats}} \sum_{k=1}^{26} f_{p,k} \mathrm{SAT}_p(x,y). \quad (2)$$

In (2), Ndays denotes the number of days in each DJF season, Npats denotes the number of SOM patterns, and $\mathrm{SAT}_p(x, y)$ is SOM pattern p (Fig. 1). We use a "hat" in $\widehat{\mathrm{SAT}}$ to signify that the SAT field constructed from (2) is not the observed SAT; rather, it is an estimate of the SAT based on the time series of best-matching SOM patterns. The frequency of occurrence $f_{p,k}$, which has one value for each DJF season, is defined as follows:

$$f_{p,k} \equiv \sum_{i=1}^{N\mathrm{days}} \frac{\delta_{p,k,i}}{N\mathrm{days}}, \quad (3)$$

and is plotted in Fig. 2 as a function of DJF season for each pattern.

Following Lee and Feldstein (2013) and Feldstein and Lee (2014), the trend in $f_{p,k}$ can be used to estimate the DJF SAT trend with the following equation:

$$\Delta\widehat{\mathrm{SAT}}(x,y) = \sum_{p=1}^{9} \Delta f_{p,k} \mathrm{SAT}_p(x,y), \quad (4)$$

where Δ denotes a trend calculated with linear regression. Equation (4) can be derived by applying Δ (i.e., linear regression) to both side of (2). In (4), $\Delta f_{p,k}$ corresponds to the trend in the frequency of occurrence of SOM pattern p.

To determine the contribution of each individual SOM pattern toward the SAT trend, in Fig. 3 the product of $\Delta f_{p,k}$ and $\mathrm{SAT}_p(x, y)$ is displayed for all patterns p. The estimated DJF SAT trend using (4), defined as the sum over all panels in Fig. 3, is shown in Fig. 4b. As can be seen by comparing Fig. 4a (the observed SAT trend) and Fig. 4b, a substantial fraction of the SAT trend is captured by (4) (the difference between Figs. 4a and 4b is shown in Fig. 4c). The implication of the similarity between Figs. 4a and 4b will be discussed more in section 3. Any discrepancies between Figs. 4a and 4b reflect the fact that SAT observations on any particular day are being "forced" to fit one of nine SOM patterns.

b. The composite method

To determine the physical processes that drive the growth and decay of the SOM patterns on intraseasonal time scales, we generate composites based on the Euclidean distance between the SOM patterns and observations. (This composite approach does not contribute to Figs. 1–5.) For the days that comprise these composites, the SAT anomaly fields have an excellent match with the SOM patterns (Fig. 1). We calculate lagged composites of each term in the thermodynamic energy equation, and then integrate this equation forward in time to determine the terms that make the largest contributions to SAT anomaly growth/decay associated with each SOM pattern. As discussed below, each SOM pattern shown in Fig. 1 can be accurately estimated by a composite of the SAT anomalies based on days when the Euclidean distance between that SOM pattern and the observed SAT anomaly field is small. (The threshold criteria for these composites will also be discussed below.)

The days with particularly small Euclidean distances, which comprise our composites, are termed events. To select

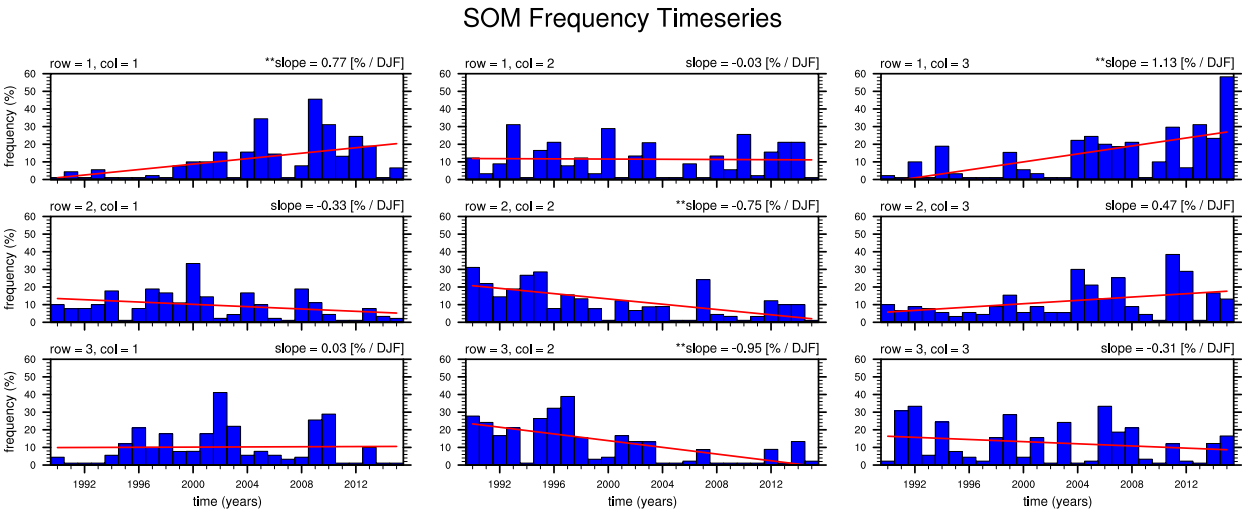

FIG. 2. The frequency of occurrence (y axis) of each self-organizing map pattern (the value of p indicates the SOM pattern number) as a function of the December–February (DJF) season (x axis). Panels correspond to the patterns shown in Fig. 1. The blue bars show the fraction of days that any particular pattern was the best-matching pattern (see text) to the daily surface air temperature anomaly field for the corresponding DJF season. The red line is the linear fit to the blue bars and the slope of the linear fit is indicated above the top-right corner of each panel. The slopes for patterns 1, 3, 5, and 8 are statistically significant at the 5% level based on a two-tailed Student's t test, as indicated by the asterisks.

these events, we first generate *candidate* events for each SOM pattern p. A candidate event is any day for which SOM pattern p is the best-matching SOM pattern to the daily SAT anomaly field. To be considered an event, however, this candidate must satisfy several additional constraints. These constraints are applied to ensure that the resulting composites both resemble the SOM patterns and comprise statistically independent events.

To guarantee a good match between the SOM patterns and the composite patterns, any candidate event for SOM pattern p must be a day for which the Euclidean distance between SOM pattern p and the daily SAT anomaly field is a local minimum (i.e., a day when the time derivative of the Euclidean distance changes sign from negative to positive). This local minimum is also constrained to have a value of less than 0.5 standard deviations of the mean Euclidean distance associated with all candidate events for SOM pattern p. To ensure statistical independence, any pair of candidate events for SOM pattern p that satisfy the above constraints must also be separated from each other by more than 12 days, unless a different SOM pattern occurs on a date between them. If a pair of candidates are too close to each other, the candidate with the smaller Euclidean distance is considered to be an event and the other candidate event is discarded. This final constraint ensures that the events comprising our composites are statistically independent because teleconnection patterns typically have a decorrelation time scale of about 10 days (e.g., Feldstein 2000), as is the case for the SOM patterns in our study (Fig. 5). In Fig. 6, the event selection method is illustrated for two individual years, where the events are marked by yellow asterisks. In general, we find that the results of this study are not sensitive to how strictly an event is defined, but we choose to utilize strict constraints in order to maximize the resemblance between the composite SAT anomalies and the corresponding SOM patterns in Fig. 1 and to ensure statistical independence.

Over all of the years between 1990 and 2016, the event selection criteria described above result in between 19 and 34 events for all SOM patterns. The resulting composite SAT anomaly fields for each SOM pattern are very similar to those displayed in Fig. 1 (not shown). Therefore, the SAT anomaly composites can be substituted in place of $\mathrm{SAT}_p(x, y)$ in (4) with little impact on the accuracy of the estimate for $\widehat{\Delta \mathrm{SAT}}(x, y)$ (not shown).

Excellent correspondence is found between the SAT anomaly SOM patterns in Fig. 1 and composites of the temperature anomalies calculated on the lowest hybrid sigma–pressure level of the ECWMF reanalysis model (see Fig. 7), which corresponds to a height of about 10 m (Berrisford et al. 2009). Therefore, to investigate the processes that drive the SAT anomalies, for each SOM pattern, as discussed above, we integrate the thermodynamic energy equation, that is,

$$\frac{\partial T'}{\partial t} = -\left(u\frac{\partial T}{\partial x}\right)' - \left(v\frac{\partial T}{\partial y}\right)' - \left(\dot{\eta}\frac{\partial T}{\partial \eta}\right)' + \left(\frac{\kappa T\omega}{p}\right)' + Q_1' + Q_2' + Q_3' + Q_4', \tag{5}$$

on the lowest hybrid sigma–pressure level, where primes signify anomalies. We calculate lagged composites of each term on the rhs of (5) for each SOM pattern. (Note that the primes on bracketed quantities apply to the product within the brackets.) We examine the thermodynamic energy equation on the lowest hybrid sigma–pressure level for a practical reason, namely that wind and diabatic heating data are not available at a height of 2 m. However, wind and

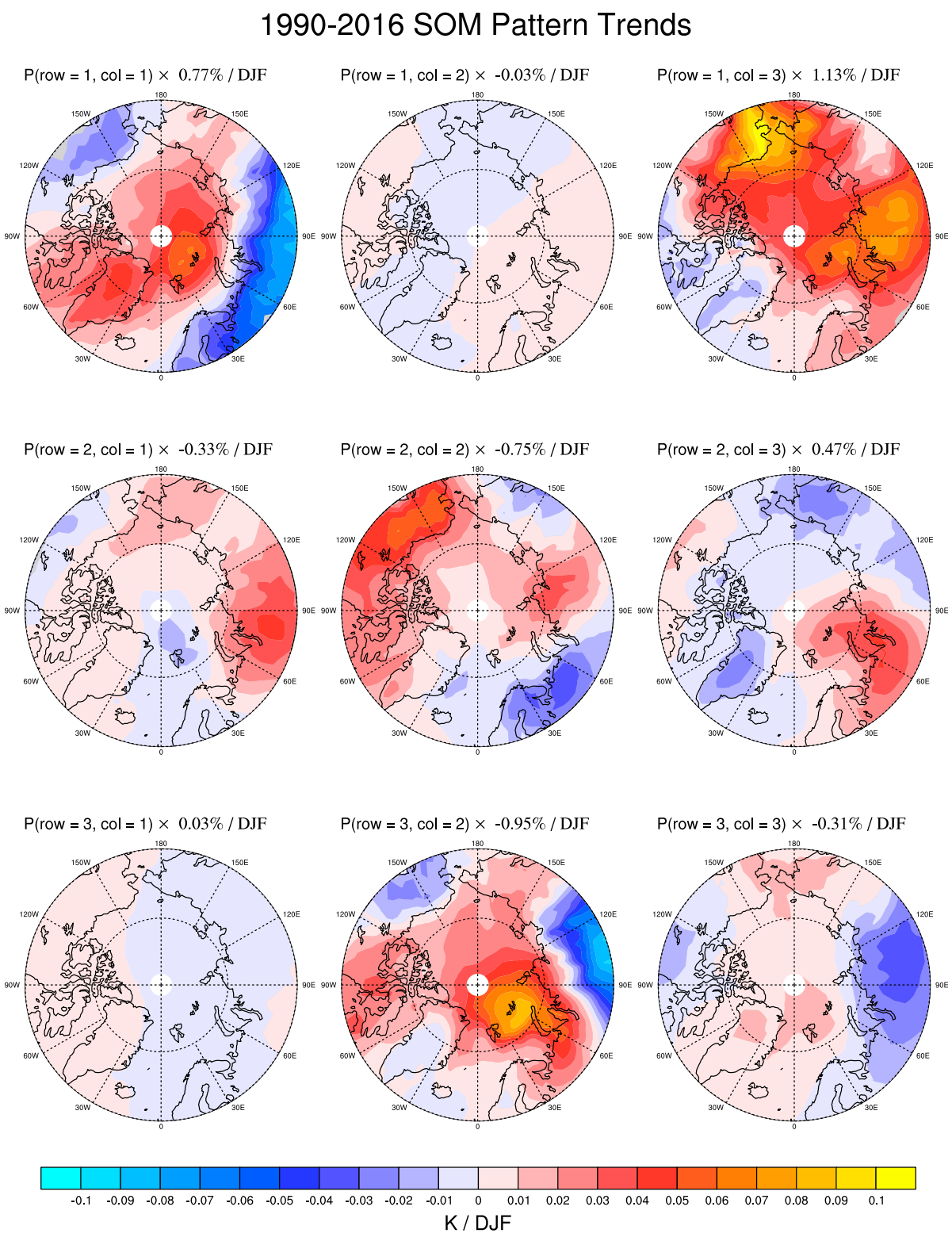

FIG. 3. The contribution to the surface (2 m) air temperature trend by each SOM pattern identified in daily data from 1990–2016 during December–February. The value of p indicates the SOM pattern number. As indicated in the top label for each panel, these contributions are calculated by multiplying the linear trend in the frequency of each pattern (Fig. 2) by the SOM patterns in Fig. 1.

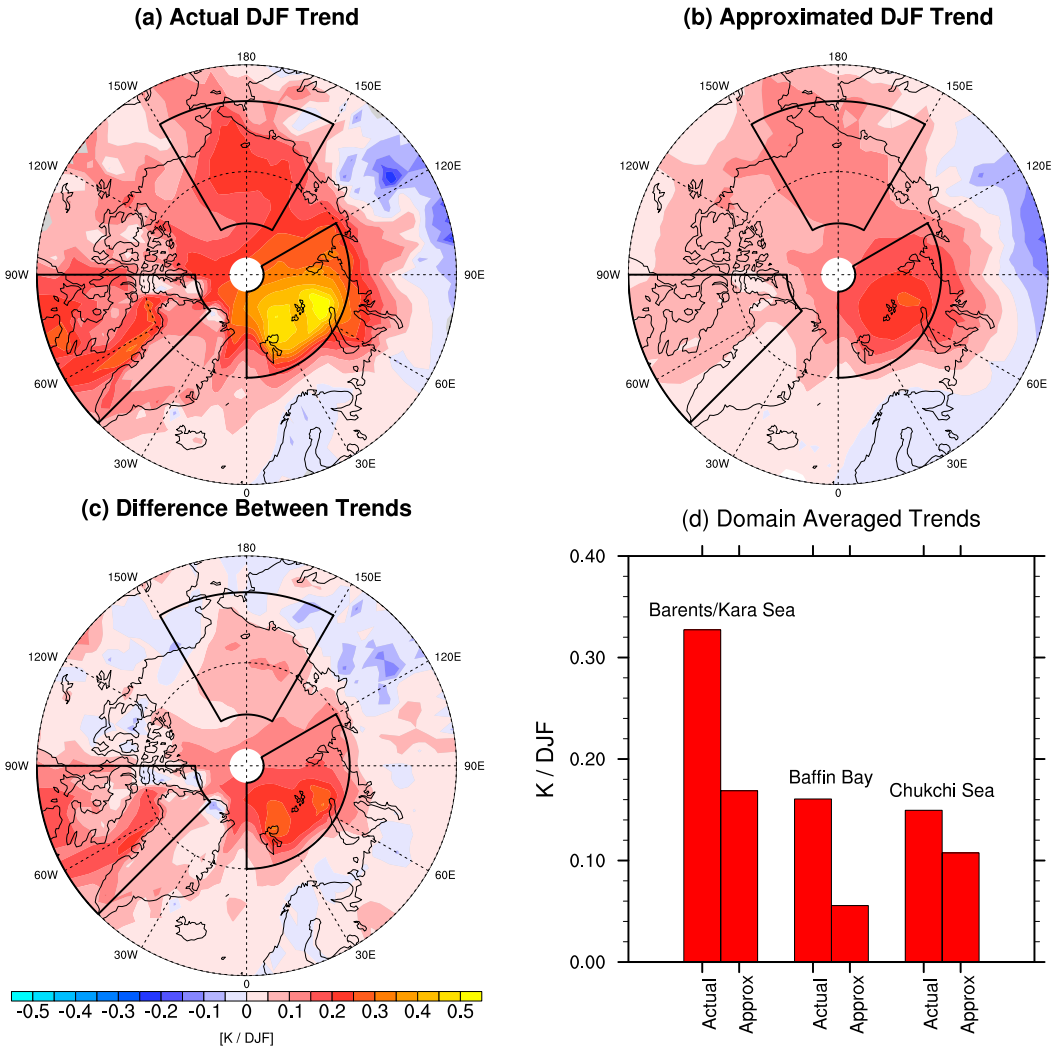

FIG. 4. (a) The observed 1990–2016 DJF surface air temperature trend. (b) The approximated (see text) 1990–2016 DJF surface air temperature trend using self-organizing maps. (c) The difference between the observed and approximated surface air temperature trends [(a) minus (b)]. (d) The values of the 1990–2016 DJF surface air temperature trends averaged in the domains outlined by boxes overlaid in (a)–(c). The average values in (d) are area weighted.

diabatic heating data are available at the lowest hybrid sigma–pressure level. Therefore, we assume that the terms that drive the temperature anomalies on this lowest hybrid sigma–pressure level are the same as those that drive the SAT anomalies.

Equation (5) shows that anomalous horizontal temperature advection, anomalous vertical temperature advection, anomalous adiabatic warming, and anomalous diabatic heating all potentially contribute to changes in the temperature anomalies T' on the lowest reanalysis model level. In this study, an anomaly is defined as the deviation from the *smoothed* calendar-day mean, which is obtained by retaining the first 10 harmonics of the seasonal cycle. As discussed in Clark and Feldstein (2020a), the horizontal temperature advection term can be decomposed further by letting $\mathbf{u} = \overline{\mathbf{u}} + \mathbf{u}'$ and $T = \overline{T} + T'$, which results in

$$\begin{aligned} -\mathbf{u}\cdot\nabla T + \overline{\mathbf{u}\cdot\nabla T} = -(\mathbf{u}\cdot\nabla T)' &= (-\mathbf{u}'\cdot\nabla\overline{T} + \overline{\mathbf{u}'\cdot\nabla\overline{T}}) \\ &+ (-\overline{\mathbf{u}}\cdot\nabla T' + \overline{\overline{\mathbf{u}}\cdot\nabla T'}) \\ &+ (-\mathbf{u}'\cdot\nabla T' + \overline{\mathbf{u}'\cdot\nabla T'}) \\ &+ (-\overline{\mathbf{u}}\cdot\nabla\overline{T} + \overline{\overline{\mathbf{u}}\cdot\nabla\overline{T}}), \end{aligned} \tag{6}$$

where overbars denote the smoothed seasonal cycle, primes denote deviation therefrom, $\nabla \equiv (\partial/\partial x, \partial/\partial y, 0)$, and $\mathbf{u} = (u, v, 0)$. Because the overbar denotes a smoothed seasonal cycle, rather than a time mean, the terms $\overline{\mathbf{u}'\cdot\nabla\overline{T}}$, $\overline{\overline{\mathbf{u}}\cdot\nabla T'}$, and $(-\overline{\mathbf{u}}\cdot\nabla\overline{T} + \overline{\overline{\mathbf{u}}\cdot\nabla\overline{T}})$ are very close to but not exactly equal to zero (Clark and Feldstein 2020a).

The diabatic terms in (5)—which, as described above, comprise radiational heating (shortwave and longwave), vertical mixing, and latent heat release—are downloaded explicitly from ERA-Interim as 12-h accumulated fields for both

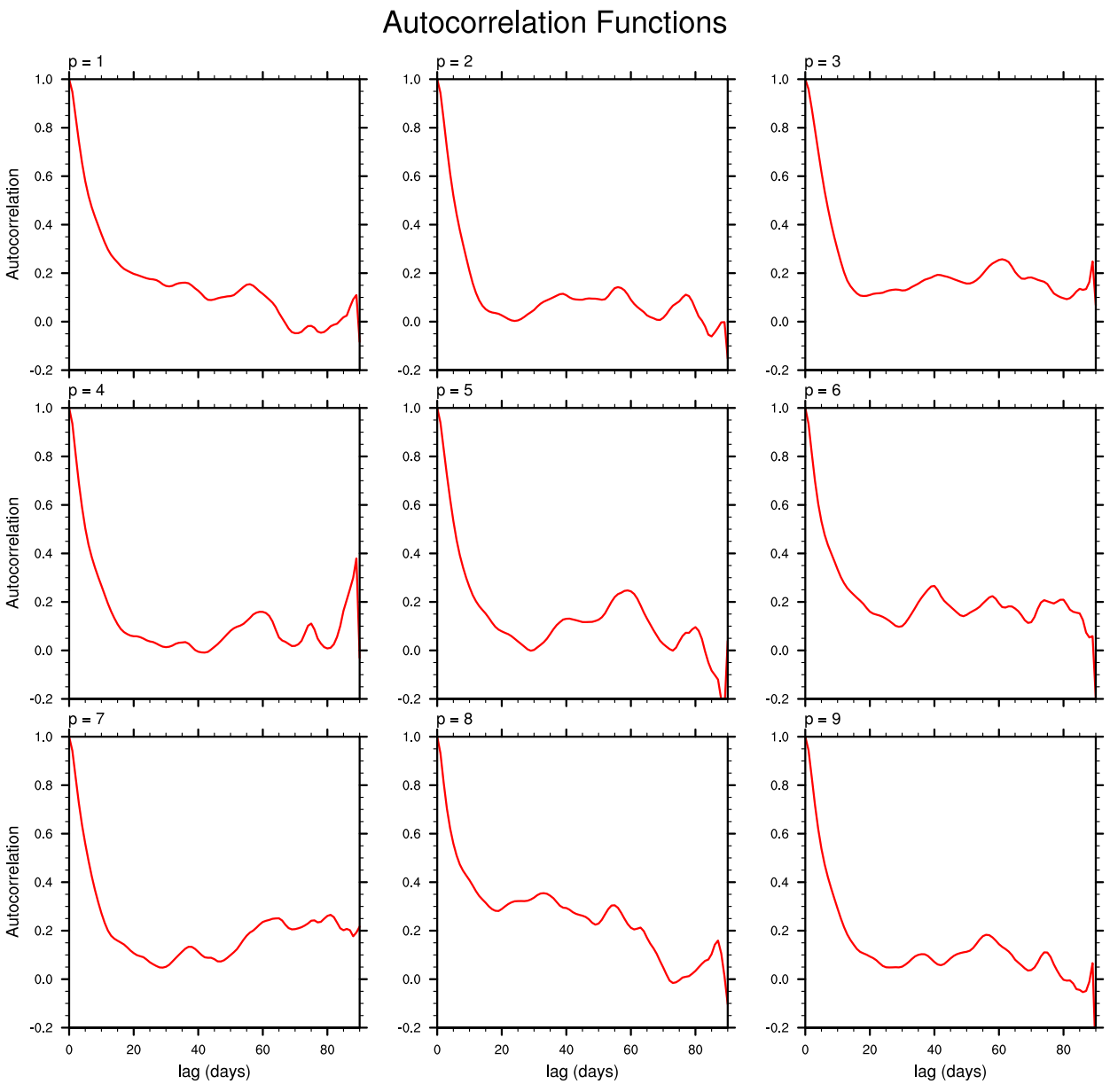

FIG. 5. Autocorrelation functions of the projection time series associated with each SOM pattern. The projection time series are obtained by calculating the dot product between the daily SAT anomaly data and the SOM patterns shown in Fig. 1.

0000 and 1200 UTC. The daily mean heating is then obtained by adding the 0000 and 1200 UTC 12-h accumulations. The horizontal temperature advection terms represent daily means, calculated with 6-hourly wind data and temperature data on the lowest model level, and applying the gradient operator in spherical form (an NCAR Command Language built-in function, gradsf, was utilized). The adiabatic warming term is also a daily mean calculated with 6-hourly data. A detailed discussion for the calculation of vertical temperature advection on the lowest model level is included in the appendix section of Clark and Feldstein (2020a). All terms in (5) and (6) are domain averaged in the green boxes outlining the dominant anomalies shown in Fig. 7. The motivation for choosing the domains in Fig. 7 will be discussed in the next section.

After domain averaging, composite values of each term in (5) and (6) are integrated forward in time starting at lag day −15, with a time step of one day, using the composite values at each lag day, following the method of Seo et al. (2016) and Clark and Feldstein (2020a,b). Specifically, after letting A denote any of the terms on the rhs of (5) or (6) averaged over a green box in Fig. 7, we compute

$$\int_{-15}^{\text{lag}} A(t)\,dt \approx \sum_{t=-15}^{\text{lag}} A(t)\,\delta t \tag{7}$$

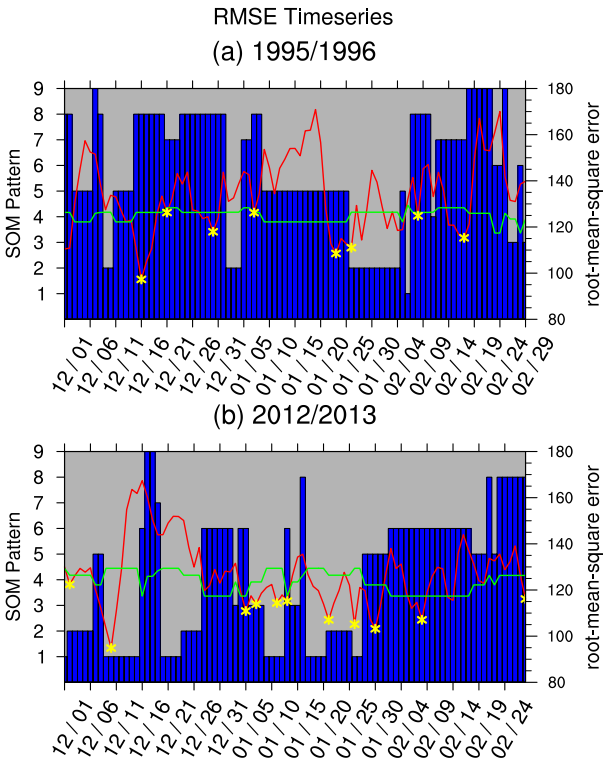

FIG. 6. The best-matching self-organizing map pattern (blue bars) and corresponding Euclidean distance to the daily surface air temperature anomaly field (red lines) for the (a) 1995/96 and (b) 2012/13 DJF seasons. The green line shows the threshold determined by the candidate events associated with the best-matching self-organizing map pattern (see section 2). Yellow asterisks are overlaid on the red line for days that were determined to be an event (see section 2).

for each term A, where lag varies between −15 and +15 days, t denotes the composite time lag in days, and δt is equal to 1 day. Each term A has units of K day^{-1}, but after integration using (7), $\sum_{t=-15}^{\text{lag}} A(t)\delta t$ has units of K and represents the contribution of term A to the temperature change; that is, $T'_A(\text{lag}) - T'_A(-15)$ for the domain under consideration, where T'_A corresponds to the temperature anomaly on the lowest hybrid sigma–pressure level associated with term A. Since $T'(-15)$ is typically found to be small, consistent with Fig. 5, and because each term in (5) is also assumed to be small at lag −15, the calculation in (7) gives an estimate of $T'(\text{lag})$ arising from term A. For lag day 0, the integration performed with (7) can be thought of as generating an estimate of the contribution by term A to the SAT anomalies of the SOM patterns. Therefore, for each term A, by substituting the integrated lag-day-0 SAT anomalies for SAT_p in (4), we can determine which of the terms in (5) and (6) make the largest contribution to the SAT trend shown in Fig. 4b. (Note that the events described above are designated to be lag day 0 in these integrations.)

As will be discussed in section 3, 15 days approximates two decorrelation time scales of each SOM pattern; however, it is found that the results are not sensitive to the day at which the integration is initiated. Statistical significance is tested with a Monte Carlo approach, by randomly generating 250 composites.

3. Results

a. *The causes of surface air temperature trends: Thermodynamic energy budget at the lowest model level*

Comparing Figs. 1 and 2, it is evident that warm Arctic SOM patterns are increasing in frequency and cold Arctic SOM patterns are decreasing in frequency. This result is unsurprising and guaranteed because the underlying data have a positive trend. Based on (4) and the results shown in Figs. 1 and 2, we expect the approximated Arctic SAT trend to be characterized by warming much like that shown in Fig. 4a. Indeed, over the Arctic, Fig. 4b shows that the approximated SAT trend strongly resembles the observed SAT trend. In fact, the approximated SAT trend in Fig. 4b is characterized not only by broad warming over the Arctic but also by a local maximum of warming over the Barents and Kara Seas, much like that seen for the observed Arctic SAT trend (Fig. 4a). Specifically, the estimated Arctic SAT trend can explain about one-half of the trend over the Barents and Kara Seas, one-third of the trend over Baffin Bay, and two-thirds of the trend over the Chukchi Sea (Fig. 4d). As discussed below, on average, about 85% of the variance of each SOM pattern comes from intraseasonal time scales. Therefore, these results indicate that in addition to an interannual-time-scale contribution to the interdecadal Arctic SAT trend, intraseasonal-time-scale weather patterns also likely make an important contribution to the driving of the trend. The SOM patterns that most strongly contribute to the SAT trend pattern shown in Fig. 4b are patterns 1, 3, 5, and 8, as seen in Fig. 3.

The fact that the estimate for the interdecadal Arctic SAT trend in Fig. 4b is a good match to the observed Arctic SAT trend in Fig. 4a has important implications. Noting that the decorrelation time scale of each SOM pattern is found to be less than about 10 days (Fig. 5), as measured by the number of days that it takes for the autocorrelation function of each SOM pattern to decay by a factor of e, the match between Figs. 4a and 4b suggests that a substantial fraction of the interdecadal Arctic SAT trend can be explained by the interdecadal trend in the frequency of occurrence of spatial patterns that have a large contribution from intraseasonal-time-scale weather. However, as will be discussed below, there is a contribution to the estimated SAT trend shown in Fig. 4b from interannual-time-scale variability that projects onto the intraseasonal-time-scale patterns. Nonetheless, the intraseasonal decay of the autocorrelations in Fig. 5 suggest that intraseasonal variability is important for driving the Arctic SAT trend. (The time series for the amplitude of each SOM pattern were obtained by projecting the daily SAT onto the SOM pattern, i.e., calculating the dot product between the daily SAT anomaly field and each SOM pattern. Note that these projections are not part of the SOM analysis.) As discussed in the introduction, these results, on their own, do not indicate whether or not the trends

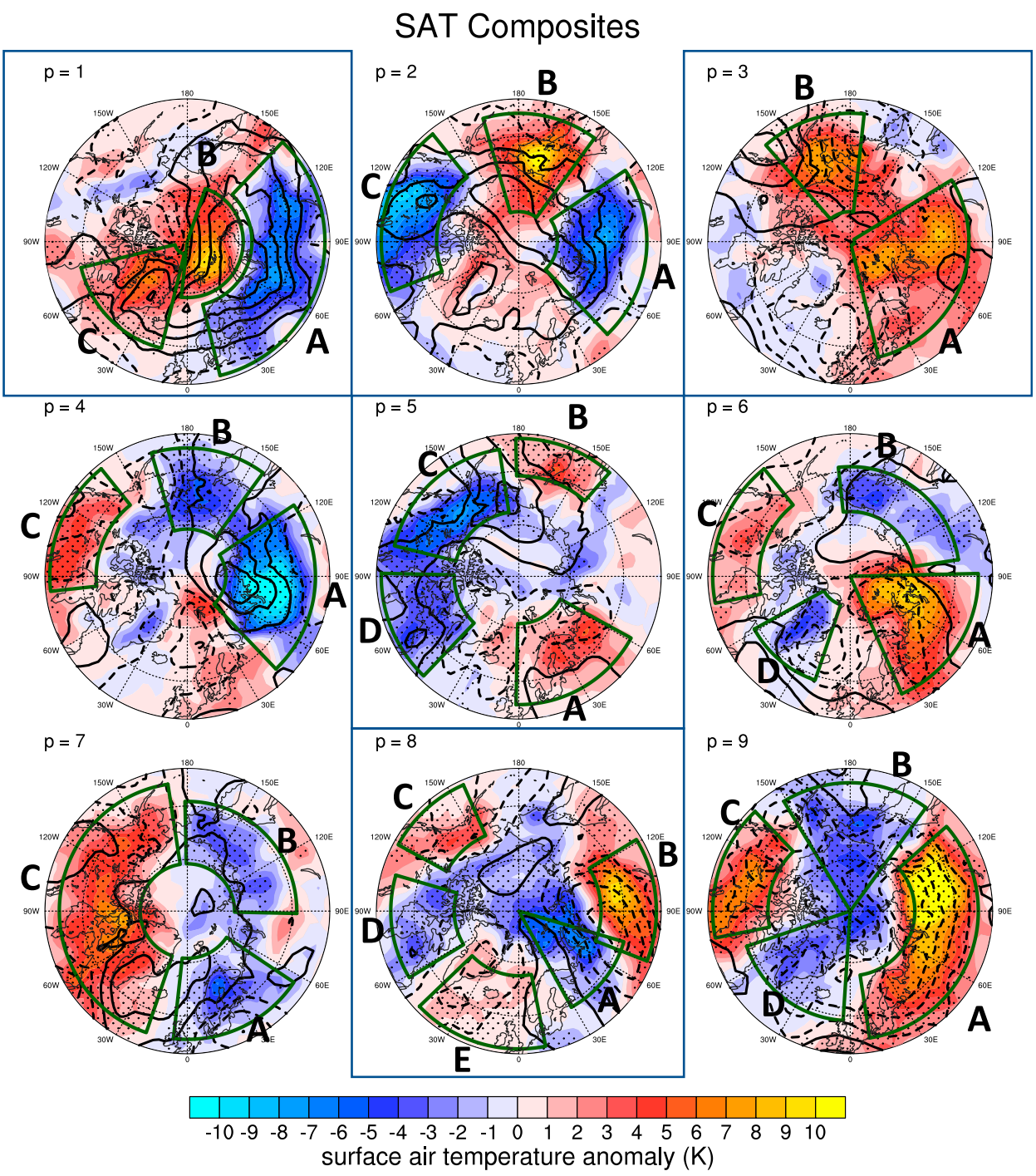

FIG. 7. Temperature anomaly composites (colors) on the lowest model level and sea level pressure anomaly composites (contours) for the self-organizing map events (see section 2). Solid (dashed) contours denote positive (negative) sea level pressure anomalies. Alphabetically labeled green boxes outline the major anomalies examined in this study (also see Fig. 8). Stippling indicates statistical significance of the surface air temperature anomaly composites for $p < 0.10$.

in the frequency of each SOM pattern arise from natural variability.

Next, we quantify the intraseasonal and interannual contribution to the SOM patterns. We use two approaches. In the first approach we remove the interannual variability from the projection time series by subtracting the DJF mean from each season. For the SOM patterns, we find that the variance of the resulting time series varies between 66% and 82% (with a

median of 76%) of the corresponding time series that includes interannual variability. The actual variance due to intraseasonal-time-scale processes is larger than these values, because seasonal-mean sampling of an intraseasonal AR(1) process can account for a substantial fraction of the interannual variance. This relationship between intraseasonal-time-scale fluctuations and interannual variance is known as climate noise (e.g., Madden 1976; Madden and Shea 1978; Feldstein 2002; Franzke 2009). A climate noise calculation was performed by computing 1000 synthetic time series, each using the lag-1-day autocorrelation of the corresponding SOM projection time series. As the median interannual variance from climate noise was found to be 44% of the total interannual variance, these results imply that, on average, intraseasonal time scales account for about 87% of the total variance. In the second approach, we reconstruct the daily SAT fields by assigning each day to the SOM pattern with the minimum Euclidean distance (as discussed in section 2a). Removing the interannual variability from the resulting SAT field, by subtracting the DJF mean from each season, shows that about 84% of the variability in the SAT is generated on intraseasonal time scales. Although these results indicate that intraseasonal-time-scale processes dominate the variance of the SOM patterns, the SOM method cannot quantify the exact fraction of the Arctic amplification trend that is explained by intraseasonal-time-scale processes. Nevertheless, these results are strongly suggestive that intraseasonal-time-scale processes play an important role in Arctic amplification.

In spite of these results, however, we recognize the importance for future research to further examine the relative importance of intraseasonal and interannual variability on Arctic amplification. It is important to note that our method is targeted toward understanding the intraseasonal contribution to Arctic warming.

To determine the processes that are contributing to the Arctic SAT trend, we next examine the thermodynamic energy budget of the SAT anomalies that characterize each SOM pattern. However, because the large number of SAT anomalies (labeled by green boxes in Fig. 7) make the examination of the thermodynamic energy budget cumbersome, for the remainder of this study, we focus only on the SOM patterns with statistically significant increasing or decreasing trends (Fig. 2). These trending SOM patterns that form the focus of the remainder of this study are patterns 1, 3, 5, and 8. SOM patterns 2, 4, 6, 7, and 9 are also examined, but are deferred to the online supplemental material.

We begin our discussion of the thermodynamic energy budget with the SAT anomaly labeled "A" (indicated by a green box over Siberia) associated with SOM pattern 1 (Fig. 7, top left). For SOM pattern 1, the SAT anomaly labeled "A" is referred to as "SOM P1: A" in Fig. 8. Although SOM P1: A is characterized by colder than average temperatures within the interior of Asia, poleward of this anomaly, within the Arctic, warmer than average temperatures are observed (Fig. 7, top left). Therefore, SOM P1 is reminiscent of the warm Arctic–cold continent SAT trend pattern observed in recent decades (e.g., Cohen et al. 2014). As discussed in the previous section, to determine what terms are driving SOM P1: A, each term in the thermodynamic energy equation, (5), is integrated forward in time using (7). The box-averaged SAT values calculated from this integration, as well as the box-averaged composite SAT anomaly itself, are shown in Fig. 8 (top left).

Upon examination of SOM P1: A (Fig. 8, top left), we can see that the SAT anomaly (thick gray line) reaches a peak value of about −4.0 K at lag day +1 (right y axis). The term in the thermodynamic energy equation that most strongly contributes to this SAT anomaly over Siberia is the anomalous horizontal temperature advection (thick red line; left y axis), which is dominated by the contribution from the anomalous wind, $(-\mathbf{u}' \cdot \nabla\overline{T} + \overline{\mathbf{u}' \cdot \nabla\overline{T}})$, shown by the thin red line. This term, which corresponds to the advection of the climatological temperature by the anomalous wind, contributes about −10 K of temperature change over the 30-day integration period for SOM P1: A. This finding, and the fact that SOM P1 has been occurring more frequently, supports the idea that changes in the large-scale circulation, and the accompanying changes in horizontal temperature advection, have contributed to the emergence of the warm Arctic–cold continent SAT pattern (Clark and Lee 2019).

The driving of the negative SAT anomaly of SOM P1: A by the term $(-\mathbf{u}' \cdot \nabla\overline{T} + \overline{\mathbf{u}' \cdot \nabla\overline{T}})$ is consistent with the fact that the SAT anomaly is located in a region where the anomalous sea level pressure gradient is maximized (see the contours in Fig. 7, top left). In addition, the vertical mixing + latent heat release term (dashed blue line) also contributes to the negative SAT anomaly of SOM P1: A. However, the contribution to the SAT anomaly by vertical mixing + latent heat release is overall much weaker than that by horizontal temperature advection.

With the exception of $(-\overline{\mathbf{u}} \cdot \nabla T' + \overline{\overline{\mathbf{u}} \cdot \nabla T'})$, the remaining terms in the thermodynamic energy equation all contribute to positive temperature changes over Siberia (SOM P1: A). The most dominant of the positive terms are the longwave heating and nonlinear horizontal temperature advection terms, $(-\mathbf{u}' \cdot \nabla T' + \overline{\mathbf{u}' \cdot \nabla T'})$. Conceptually, the longwave heating term can be approximated using a linearization of the radiative transfer equation

$$\frac{Q_{\mathrm{lw}}}{c_p} \approx -\tau^{-1} T', \tag{8}$$

where τ is a relaxation time scale and T' is the SAT anomaly (Fueglistaler et al. 2009). From this perspective, a temperature anomaly decays from emission of longwave radiation, resulting in a dampening of the SAT anomalies that are caused by the advection of the climatological temperature by the anomalous wind. Therefore, for SOM P1: A, while the advection of the climatological temperature by the anomalous wind drives the growth of the SAT anomaly, the longwave heating drives its decay. A similar finding has been reported for the SAT changes associated with the NAO (Clark and Feldstein 2020a).

For SOM P1: A, the sum of all the integrated terms in the thermodynamic energy equation (thin gray line in Fig. 8) is almost equal to the temperature change (thick gray line). This confirms that our breakdown of the thermodynamic energy equation is reasonable at this location. However, for other regions examined in Fig. 8, there are often discrepancies

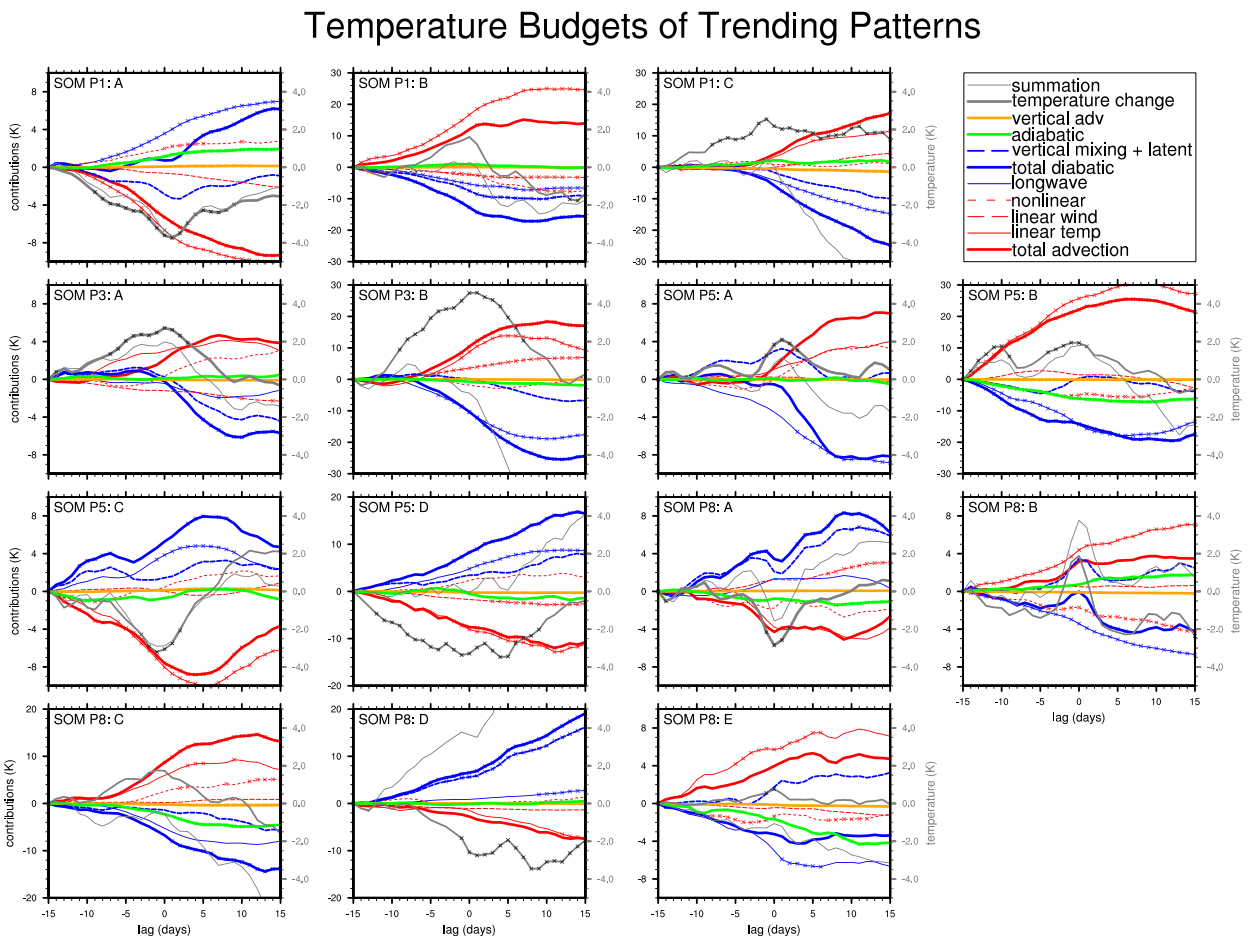

FIG. 8. (top to bottom) Thermodynamic energy budgets of the alphabetically labeled surface air temperature (SAT) anomalies shown in Fig. 7 for patterns 1, 3, 5, and 8, respectively. Each panel corresponds to a different surface air temperature anomaly boxed in green in Fig. 7. The curves in each panel correspond to different terms in the thermodynamic energy equation (see legend). The thick gray line corresponds to the domain (area-weighted)-average SAT anomaly composite minus the lag day −15 SAT anomaly. The remaining terms (also domain averaged) are $-\mathbf{u}\cdot\nabla T+\overline{\mathbf{u}}\cdot\nabla\overline{T}$ (thick red), $-\mathbf{u}'\cdot\nabla\overline{T}+\overline{\mathbf{u}'\cdot\nabla T}$ (thin red), $-\overline{\mathbf{u}}\cdot\nabla T'+\overline{\mathbf{u}}\cdot\nabla T'$, (dashed red) $-\mathbf{u}'\cdot\nabla T'+\overline{\mathbf{u}'\cdot\nabla T'}$ (dotted red), anomalous adiabatic warming/cooling (green), anomalous vertical advection (yellow), anomalous diabatic heating (thick blue), longwave heating/cooling (thin blue), vertical mixing + latent heating (dashed blue), and the sum of diabatic term with the advection terms and adiabatic warming (thin gray). The gray lines correspond to the right y axis, while the remaining terms correspond to the left y axis. Note that all terms that appear on the right-hand side of the thermodynamic energy equation, (5), are integrated using the composite values at each lag (x axis). Statistical significance at $p < 0.10$ is indicated with × marks.

between the thick and thin gray lines, most likely due to the fact that the temperature changes associated with individual terms in the thermodynamic energy equation can be an order of magnitude greater than the observed change in temperature. As a result, small numerical errors in the calculations of the dominant terms on the rhs of (5) can lead to larger errors in the summation curve (thin gray line) relative to the observed temperature change (thick gray line). Sources of error in the calculation of the dominant terms include the following:

- The use of a 24-h time step in our integration of daily mean quantities, which is significantly larger than the reanalysis time step of about 12 min (ECMWF 2014).
- The use of a horizontal resolution (2.5°) that is significantly coarser than that of the reanalysis model, which integrates the thermodynamic equation with the spectral transform method (ECMWF 2014).
- The lack of a horizontal diffusion term in our analysis, which is present in the reanalysis model but is not available for download from ECMWF or easily applied to observations (ECMWF 2014).
- The absence in our budgets of an analysis increment that is generated by ECMWF from 12-hourly data assimilation.
- The use of diabatic heating terms that represent the daily average of 12-min time steps, which differs from the daily average of 6-hourly data that was used in the other terms.

Considering these sources of error, which are often insurmountable or unavoidable, a balanced budget is not expected to occur over most regions. Nevertheless, it is still useful to

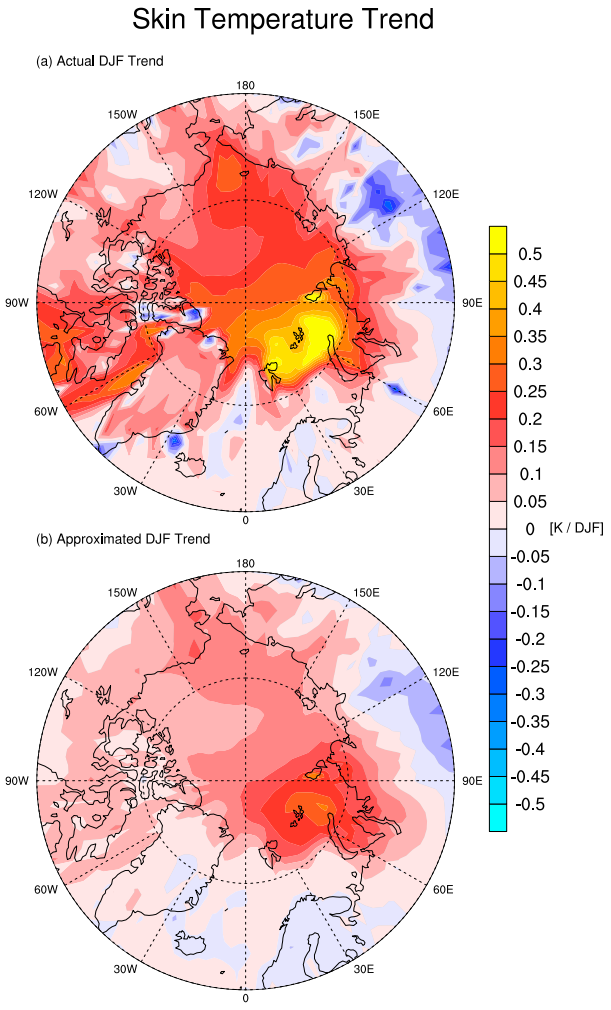

FIG. 9. (a) The observed 1990–2016 DJF skin temperature trend. (b) The approximated (see text) 1990–2016 DJF SKT trend using self-organizing maps.

examine the dominant terms in the thermodynamic budgets with these sources of error in mind.

Upon examination of the remaining panels in Fig. 8, a similar picture to that seen for SOM P1: A emerges. Specifically, the advection of the climatological temperature by the anomalous wind plays a central role in driving the growth of each SAT anomaly shown in Fig. 7, while longwave heating/cooling plays a crucial role in the decay of each SAT anomaly. This can be seen in Fig. 8 by the fact that the sign of the temperature curve (thick gray line) is usually the same as the sign of the horizontal temperature advection curve (thick red line). Furthermore, for all domains, vertical advection and adiabatic warming are unimportant contributors to the SAT anomalies relative to the other terms in the thermodynamic energy equation. However, unlike that seen for SOM P1: A, vertical mixing + latent heat release does not consistently contribute to the growth of SAT anomalies. In fact, vertical mixing + latent heat release more often contributes to the decay of SAT anomalies. For example, for SOM P1: B, SOM P3: A, SOM P8: A, and SOM P8: D, vertical mixing + latent heat release plays an even more important role in the decay of the SAT anomalies than does longwave heating/cooling. Vertical mixing + latent heat release only contributes to the growth of four SAT anomalies: SOM P1: A, SOM P5: A, SOM P8: B, and SOM P8: E.

The finding that vertical mixing contributes to the growth of only four SAT anomalies is in contrast with the sea ice albedo feedback mechanism for Arctic amplification, which predicts the growth of SAT anomalies to be dominated by vertical mixing in regions of pronounced sea ice decline. In addition, inspection of the location of these four SAT anomalies in Fig. 7 (SOM P1: A, SOM P5: A, SOM P8: B, and SOM P8: E) indicates that vertical mixing contributes to the driving of SAT changes only over continents and open ocean, where sea ice is not present climatologically.

In all but one instance (SOM P5: A), advection of the climatological temperature by the anomalous wind is the dominant contributor to SAT anomaly growth. As discussed for SOM P1: A, this finding is consistent with the fact that the SAT anomalies shown in Fig. 7 tend to be largest in regions where the amplitude of the anomalous sea level pressure gradient maximizes. In the one instance where temperature advection does not dominate the driving of the SAT anomaly, for SOM P5: A, it is vertical mixing + latent heat release that dominates the driving of the SAT anomaly.

According to the ice albedo feedback mechanism, as discussed in section 1, the melting of Arctic sea ice will result in an upward sensible and latent heat flux, in addition to an upward longwave radiative flux, followed by widespread warming over much of the Arctic. Since the sea ice melting will be confined to a relatively small region within the Arctic, the corresponding warming must be initially confined to the same small region, and the widespread warming over the Arctic that follows the sea ice melting must be accomplished by horizontal temperature advection. If this scenario has been taking place, however, we would expect to see strong contributions to the horizontal temperature advection from $(-\overline{\mathbf{u}}\cdot\nabla T' + \overline{\overline{\mathbf{u}}\cdot\nabla T'})$ and/or $(-\mathbf{u}'\cdot\nabla T' + \overline{\mathbf{u}'\cdot\nabla T'})$ (i.e., horizontal temperature advection associated with the SAT anomalies). However, our findings show that advection of the climatological temperature by the anomalous wind $(-\mathbf{u}'\cdot\nabla\overline{T} + \overline{\mathbf{u}'\cdot\nabla\overline{T}})$ dominates the SAT changes. This finding provides further support to the perspective that surface heat fluxes are not important contributors to the fraction of the Arctic SAT trend shown in Fig. 4b.

b. *The causes of skin temperature trends: The surface energy budget*

In section 2 and section 3a, we showed that a substantial fraction of the SAT trend is driven by the trend in the frequency of occurrence of the nine SOM patterns (Fig. 2). In Fig. 9b, we show that the trend in the frequency of the nine SOM patterns (Fig. 2) can also explain a substantial fraction of the total SKT trend, since substitution of the SKT anomaly composites (Fig. 10 and Fig. S2 in the online supplemental material, leftmost column) in place of $\mathrm{SAT}_p(x, y)$ in (4) leads

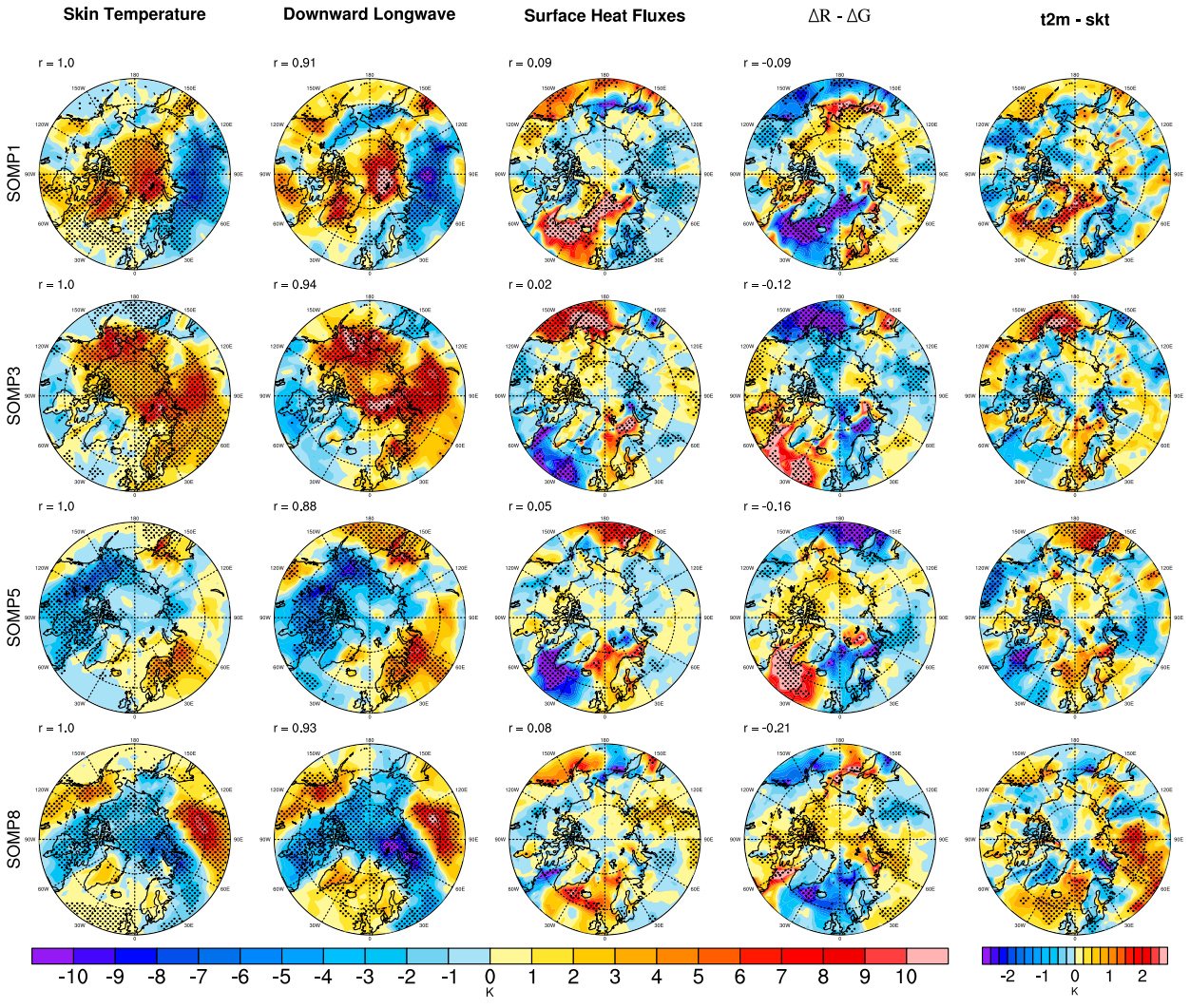

FIG. 10. (top to bottom) Composite surface energy budget for self-organizing map patterns 1, 3, 5, and 8, respectively. (left to right) Lag-day-0 composites of the skin temperature anomaly, surface downward longwave radiation anomaly, surface (latent + sensible) heat flux anomaly, residual, and the 2-m temperature anomaly minus the skin temperature anomaly, respectively. The pattern correlation with the corresponding skin temperature anomaly pattern is indicated in the top-left corner of each panel (except for the rightmost column, which does not appear in the surface energy budget equation). Each quantity of the surface energy budget represents a daily mean. Statistical significance at $p < 0.10$ is indicated by the stippling.

to a good match with the observed SKT trend (Fig. 9a). To determine what processes are contributing to the SKT trend shown in Fig. 9b, we derive an equation for the evolution of SKT anomalies.

Letting F_{lw}, F_{sw}, and F_h denote the longwave radiative flux, shortwave radiative flux, and surface heat flux (latent + sensible), respectively, and R a residual, the surface energy budget can be written as

$$G = F_{\mathrm{lw}}^{\downarrow} + F_{\mathrm{lw}}^{\uparrow} + F_{\mathrm{sw}}^{\downarrow} + F_{\mathrm{sw}}^{\uparrow} + F_h + R, \tag{9}$$

where $G\{\equiv\int_0^{\Delta z}\rho c_p(dT/dt)dz\}$ denotes energy storage within a thin surface layer of depth Δz, $\downarrow$ denotes a downward flux, and $\uparrow$ denotes an upward flux. Taking the differential δ to represent an anomaly, defining a downward flux as positive, and letting $F_{\mathrm{lw}}^{\uparrow} = -\varepsilon_s\sigma T_s^4$, where T_s is the skin temperature, σ is the Stefan–Boltzmann constant, and ε_s is the surface emissivity, the surface energy budget can be expressed in terms of anomalies:

$$\delta G = \delta F_{\mathrm{lw}}^{\downarrow} - 4\varepsilon_s\sigma\{T_s\}^3\delta T_s + \delta F_{\mathrm{sw}}^{\downarrow} + \delta F_{\mathrm{sw}}^{\uparrow} + \delta F_h + \delta R, \tag{10}$$

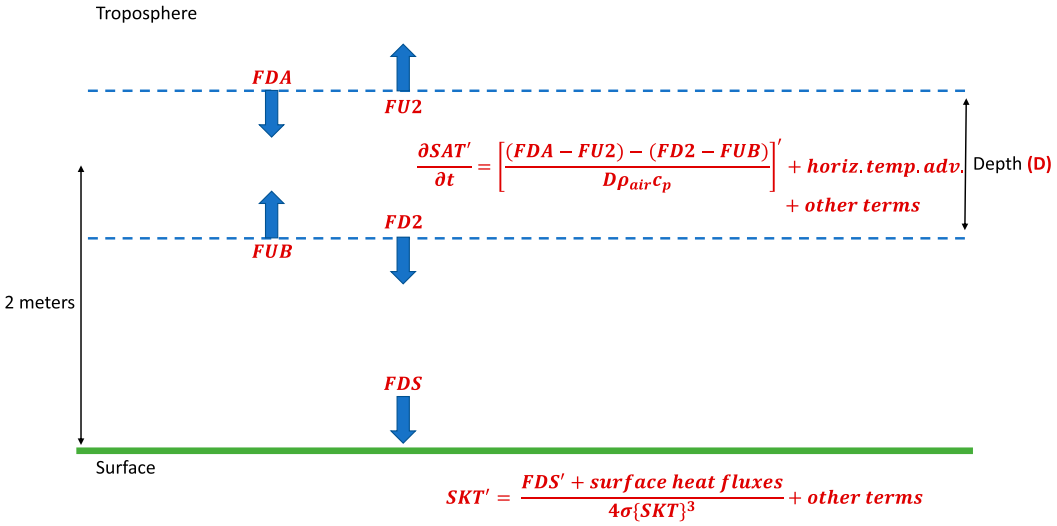

FIG. 11. Idealized schematic illustrating how longwave radiative fluxes impact the surface air temperature (SAT) and skin temperature (SKT). At a height of 2 m, a layer of depth D is depicted with a temperature (SAT) that is impacted by downward longwave fluxes entering the top of the layer (FDA) and exiting the bottom of the layer (FD2). The temperature of the layer at 2 m is also impacted by upward longwave fluxes entering the layer from the bottom (FUB) and exiting from the top (FU2). The SKT is impacted by only one longwave flux, which is the downward longwave flux at the surface (FDS). The SAT is a fluid and is impacted also by horizontal temperature advection, as indicated, while the SKT can only be impacted by upward or downward fluxes, or other residual processes, as discussed in the text.

where curly braces denote DJF climatology. After rearranging terms, we arrive at an expression for the skin temperature anomaly δT_s:

$$\delta T_s = \frac{\delta F_{\mathrm{lw}}^{\downarrow} + \delta F_h + \delta R - \delta G}{4\varepsilon_s \sigma \{T_s\}^3} \tag{11}$$

(Lu and Cai 2009; Lesins et al. 2012; Gong et al. 2017; Lee et al. 2017; Clark and Feldstein 2020a). Shortwave radiative fluxes are neglected (because it is dark during DJF over the Arctic) and the surface emissivity ε_s is set equal to one. Each term in (11) is plotted in Fig. 10 (columns) for the four trending SOM patterns (rows) and in Fig. S2 for the remaining SOM patterns (2, 4, 6, 7, and 9). In both Fig. 10 and Fig. S2, the quantity $\delta R - \delta G$ is treated as a residual, which includes vertical mixing and horizontal temperature advection within the ocean, conduction through soil, sea ice, and snow, and latent heating associated with the melting and freezing of sea ice and snow.

Compared to all other terms in (11), the surface DLR anomalies most strongly resemble the SKT anomalies (Fig. 10), with a pattern correlation of about 0.90 for all SOM patterns. The pattern correlations between the SKT and all other terms in the surface energy budget (i.e., the surface heat fluxes and residual) are substantially smaller. In light of the strong correlation between the DLR and SKT anomaly patterns, one can ask whether the SKT anomalies are caused by the DLR anomalies or vice versa. We can gain insight into this question by considering the other terms in the surface energy budget. For regions where there are positive SKT anomalies, if the SKT were to increase the DLR, a flux of heat from the surface to the atmosphere must occur. Therefore, if such a process were occurring in observations, we would expect to see upward (negative) surface heat fluxes in regions of positive SKT anomalies. However, for all four SOM patterns in Fig. 10, the correlations between the SKT field and the surface heat fluxes are positive (downward surface heat fluxes over regions with positive SKT anomalies). In addition, if the SKT were not driven by the fluxes from the atmosphere, then the SKT would be driven by residual processes. Contrastingly, for all four SOM patterns in Fig. 10, the residual is negatively correlated with the SKT anomaly pattern. These results imply that the surface DLR anomalies likely drive the SKT anomalies, not the other way around. In addition, these results also indicate that DLR is the primary driver of the SKT trend shown in Fig. 9b. However, we must emphasize that, although DLR is driving the SKT anomalies, DLR is not driving the SAT anomalies. As discussed in the previous subsection, SAT anomalies are driven primarily by horizontal temperature advection.

One may ask why longwave radiation drives temperature anomaly growth at the surface (Fig. 10), but the temperature anomaly decays at only 2 m above the surface (Fig. 8). The reason is illustrated schematically in Fig. 11. At the surface, as seen in Fig. 11, longwave radiation contributes to temperature changes solely through absorption of downward longwave radiation (DLR). In contrast, above the surface, the longwave radiation Q_1 has contributions from the absorption of both downward and upward longwave radiation, as well as from the emission of downward and upward longwave radiation.

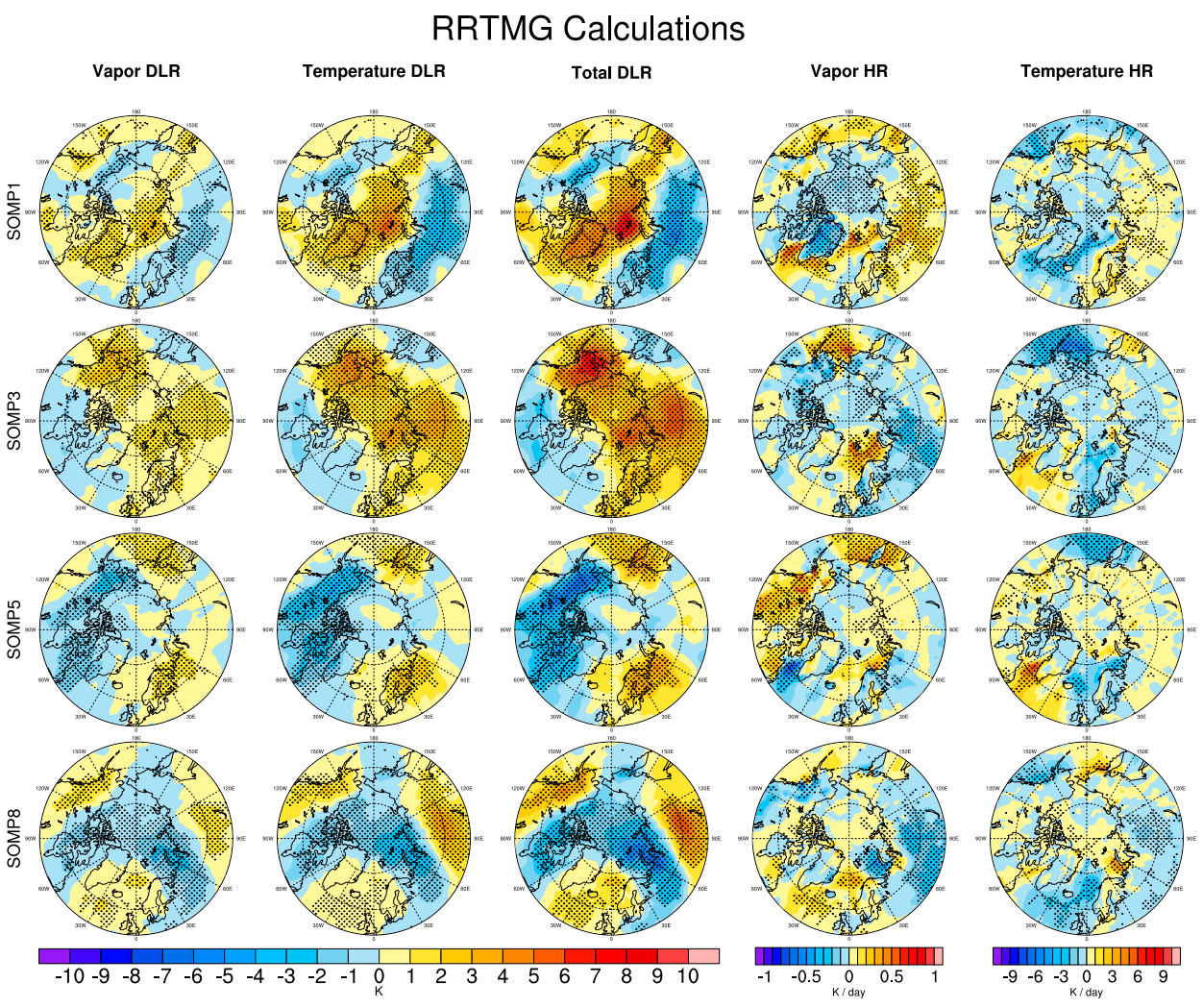

FIG. 12. The contribution to the skin temperature anomalies from (column 1) water vapor–driven DLR and (column 2) temperature-driven DLR. (column 3) The sum of columns 1 and 2. Also shown are (column 4) the water vapor–driven and (column 5) the temperature-driven longwave radiative heating rates at the lowest reanalysis model level.

We examine what is driving the longwave radiation at both the surface and 2 m above the surface using the Rapid Radiative Transfer Model (RRTMG; Mlawer et al. 1997; Iacono et al. 2008). In particular, we follow Clark and Feldstein (2020b) and conduct two types of clear-sky radiative transfer calculations. The aim of the first (second) calculation is to determine the contribution that atmospheric temperature (moisture) anomalies have on both the surface DLR and the radiative heating rates on the lowest model level. The first (second) calculation is conducted by inputting the observed temperature and climatological water vapor concentrations (climatological temperature and observed water vapor concentrations) for the entire depth of the atmosphere into RRTMG. For more details about configuring the data for these calculations, see Clark and Feldstein (2020b) and their supplementary material.

After performing RRTMG calculations to determine the anomalous surface DLR and radiative heating rates, composites of surface DLR and radiative heating rate anomalies are calculated for the events discussed in section 2 (Fig. 12 and Fig. S4). The leftmost three columns of Fig. 12, respectively, show the water vapor–driven contribution to the surface DLR anomalies, the temperature-driven contribution to the surface DLR anomalies, and their summation (column 1 + column 2). The summation of column 1 and 2 is an excellent match with the ERA-Interim clear-sky DLR anomalies (cf. Fig. 12, column 3, to the corresponding SOM patterns in Fig. S3), indicating that the contributions from temperature and water vapor anomalies to the surface DLR anomalies can be linearly separated. As shown in Fig. 12, the dominant contributor to the clear-sky surface DLR is temperature, but water vapor is certainly also important.

To quantify the impact that cloud liquid water and ice have on the surface DLR patterns shown in Fig. 9 and Fig. S2, in Fig. 13 we show the difference between the ERA-Interim all-

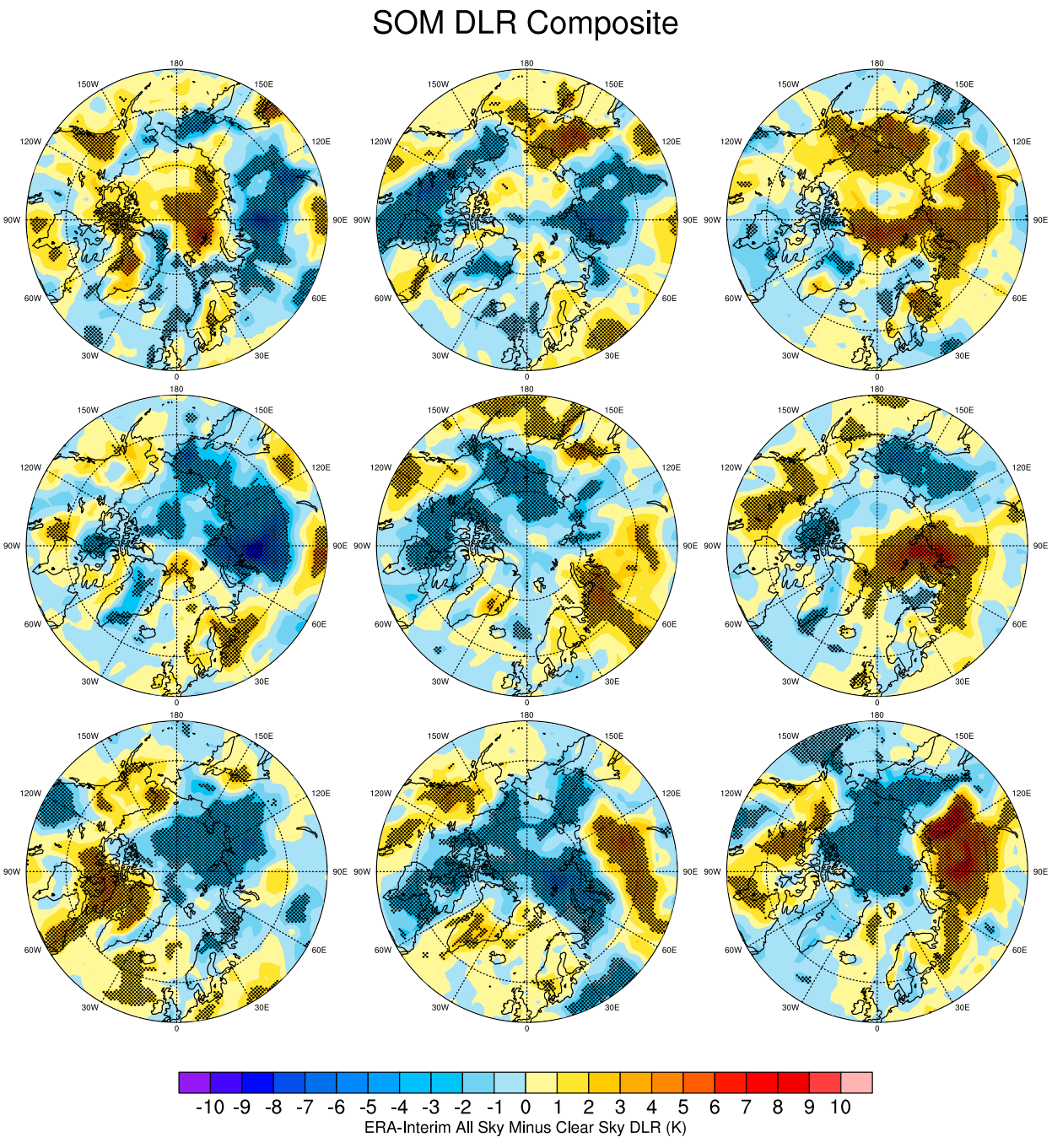

FIG. 13. The difference between surface clear-sky downward longwave radiation and surface all-sky downward longwave radiation, using ERA-Interim data.

sky and clear-sky surface DLR anomalies (i.e., subtracting the surface DLR anomalies in Fig. S3 from those in column 2 of Fig. 9 and Fig. S2). The result shows that clouds overall amplify the surface DLR anomalies; compare Fig. 13 to the corresponding patterns in Fig. 11 and Fig. S4, column 3. The impact of clouds on surface DLR identified here may also be underestimated due to inaccurate parameterizations of ice nuclei over the Arctic (e.g., Prenni et al. 2007).

As was seen for the surface DLR, the contribution to the heating rates by water vapor and temperature anomalies can be linearly separated, because the sum of the rightmost two columns is almost exactly equal the total longwave heating rates calculated by ERA-Interim (not shown). Because longwave radiation drives the decay of the lowest-model-level temperature anomalies (Fig. 8), anomalous emission must exceed anomalous absorption. Therefore, as evidenced by Fig. 12

(rightmost two columns), the emission of longwave radiation at the lowest model level is driven primarily by temperature anomalies, providing further justification for the conceptualization using (8). Interestingly, the water vapor–driven contribution to the longwave heating rate sometimes contributes to SAT anomaly growth, but the amplitude is small (Fig. 12, column 4).

Returning to the remaining panels of Fig. 10, we conclude this subsection by considering the surface heat fluxes, which have been implicated as potential contributors to Arctic amplification due to amplified sea ice decline. Apart from showing that the SKT anomalies of each SOM pattern are driven by anomalies in surface DLR, Fig. 10 also shows that the surface heat fluxes are driven in large part by the difference between the SKT and SAT anomalies (cf. Fig. 10, columns 3 and 5). This implies that the surface heat flux anomaly patterns shown in Fig. 10 can be explained by horizontal temperature advection because the SAT anomalies are driven directly by horizontal temperature advection, as shown in Fig. 8, and the SKT anomalies are, in large part, driven indirectly by horizontal temperature advection through the changes in surface DLR. Changes in moisture also impact the SKT through changes in surface DLR (Figs. 11 and 12) and although we did not examine what drives the moisture changes, it is likely that the circulation plays a prominent role here as well. The circulation changes associated with the SOM patterns would presumably also act to advect the climatological moisture field, which has a similar gradient field to that of the climatological temperature. All of these results highlight the prominent role that the circulation has on Arctic SKT variability.

4. Summary and conclusions

Although Arctic amplification is a phenomenon that is observed on interdecadal time scales, this study shows that a significant fraction of Arctic amplification can be explained by the trend in the frequency of occurrence of nine SOM patterns. These SOM patterns are shown to have a large intraseasonal contribution, as their autocorrelation functions decay significantly within a season, and on average about 85% of the variance of each SOM pattern comes from intraseasonal time scales. The warm Arctic patterns, identified by SOM analysis, are increasing in their frequency of occurrence, while the cold Arctic patterns are decreasing in their frequency of occurrence. By taking into account the trend in the frequency of occurrence of each SOM pattern, it is found that these predominantly intraseasonal-time-scale SOM patterns can explain about one-half of the observed warming trend in the Barents and Kara Seas, about one-third of the observed warming trend around Baffin Bay, and about two-thirds of the observed warming trend in the Chukchi Sea. Although this study shows that the trend in the frequency of the SOM patterns can account for a large fraction of the interdecadal SAT trend, it does not show why the frequencies of the SOM patterns have changed. An important question, which we leave for future work, is determining whether or not externally forced changes in the weather (i.e., externally forced intraseasonal variations) contributed importantly to the frequency trends of the SOM patterns.

In contrast with the viewpoint that sea ice loss is driving wintertime Arctic amplification through upward surface heat fluxes, this study suggests somewhat the opposite. At least for the contributions from the intraseasonal processes represented by the SOM patterns, horizontal temperature advection, which drives the Arctic SAT trend, is more likely the driver of the surface heat fluxes. An examination of different terms that contribute to the horizontal temperature advection reveals that the SAT anomalies of nearly all of the SOM patterns are driven by the advection of the climatological temperature field by the anomalous wind. This implies that the Arctic SAT trend has an important contribution to its trend by changes in the circulation. Whether these circulation changes are natural or a response to external forcing is not clear from the results presented in this study. Nonetheless, the finding that the circulation is driving warming over the Arctic is consistent with several observational studies (e.g., Sorokina et al. 2016; Gong et al. 2017; Lee et al. 2017), but inconsistent with a number of studies that examine the Arctic SAT response in climate model runs with sea ice removed. Perhaps the inconsistency between this study and those climate modeling studies is due to the experimental designs of the climate modeling studies. That is, the removal of sea ice in the models raises the SKT which ensures an upward heat flux. However, we also cannot rule out the possibility that the fraction of the Arctic SAT trend unexplained by the SOM patterns is driven by sea ice loss.

As a final point, this study shows that the surface energy budget should be applied strictly to the SKT, rather than to the SAT, because the equations that govern SKT changes and SAT changes are different. The SKT is the temperature of Earth's surface, which is often a solid, while the SAT is defined as the temperature of the atmosphere (i.e., a fluid) about 2 m above Earth's surface. Therefore, although the surface energy budget is a useful diagnostic tool for understanding climate variability, applying the surface energy budget as a means to understand SAT may lead to misleading results because there are no temperature advection terms in the surface energy budget equation. As shown in this study, SKT anomaly growth is driven by surface DLR, which is due to both atmospheric temperature anomalies and moisture anomalies. However, at 2 m above the surface, the SAT anomaly growth is driven by horizontal temperature advection, and longwave radiation instead contributes to SAT anomaly decay.

In spite of the fact that SKT and SAT anomaly patterns often have high spatial correspondences, as shown in this study, the horizontal temperature advection term is very important, even at levels near the surface where the winds tend to be weakest. Therefore, future studies should take care to consider the difference between what drives the SKT and what drives the SAT.

Acknowledgments. We thank Mingyu Park and Dong Wan Kim for helpful research discussions, in addition to three anonymous reviewers. This study was initiated as Vivek Shenoy's undergraduate research project at Pennsylvania State University with

Steven Feldstein. This study was supported by National Science Foundation Grants OPP-1723832 and AGS-1822015.

REFERENCES

Armour, K. C., N. Siler, A. Donohoe, and G. H. Roe, 2019: Meridional atmospheric heat transport constrained by energetics and mediated by large-scale diffusion. *J. Climate*, **32**, 3655–3680, https://doi.org/10.1175/JCLI-D-18-0563.1.

Baggett, C., S. Lee, and S. Feldstein, 2016: An investigation of the presence of atmospheric rivers over the North Pacific during planetary-scale wave life cycles and their role in Arctic warming. *J. Atmos. Sci.*, **73**, 4329–4347, https://doi.org/10.1175/JAS-D-16-0033.1.

Bekryaev, R. V., I. V. Polyakov, and V. A. Alexeev, 2010: Role of polar amplification in long-term surface air temperature variations and modern Arctic warming. *J. Climate*, **23**, 3888–3906, https://doi.org/10.1175/2010JCLI3297.1.

Berrisford, P., D. P. Dee, M. Fielding, M. Fuentes, P. W. Kallberg, S. Kobayashi, and S. Uppala, 2009: The ERA-Interim archive. ERA Rep. Series 1, 16 pp.

Budyko, M. I., 1969: The effect of solar radiation variations on the climate of the earth. *Tellus*, **21**, 611–619, https://doi.org/10.3402/tellusa.v21i5.10109.

Chylek, P., C. K. Folland, G. Lesins, M. K. Dubey, and M. Wang, 2009: Arctic air temperature change amplification and the Atlantic Multidecadal Oscillation. *Geophys. Res. Lett.*, **36**, L14801, https://doi.org/10.1029/2009GL038777.

Clark, J. P., and S. Lee, 2019: The role of the tropically excited Arctic warming mechanism on the warm Arctic cold continent surface air temperature trend pattern. *Geophys. Res. Lett.*, **46**, 8490–8499, https://doi.org/10.1029/2019GL082714.

——, and S. B. Feldstein, 2020a: What drives the North Atlantic Oscillation's temperature anomaly pattern? Part I: The growth and decay of the surface air temperature anomalies. *J. Atmos. Sci.*, **77**, 185–198, https://doi.org/10.1175/JAS-D-19-0027.1.

——, and ——, 2020b: What drives the North Atlantic Oscillation's temperature anomaly pattern? Part II: A decomposition of the surface downward longwave radiation anomalies. *J. Atmos. Sci.*, **77**, 199–216, https://doi.org/10.1175/JAS-D-19-0028.1.

Cohen, J., and Coauthors, 2014: Recent Arctic amplification and extreme mid-latitude weather. *Nat. Geosci.*, **7**, 627–637, https://doi.org/10.1038/ngeo2234.

Compo, G. P., and P. D. Sardeshmukh, 2009: Oceanic influences on recent continental warming. *Climate Dyn.*, **32**, 333–342, https://doi.org/10.1007/s00382-008-0448-9.

Dai, A., D. Luo, M. Song, and J. Liu, 2019: Arctic amplification is caused by sea-ice loss under increasing CO_2. *Nat. Commun.*, **10**, 121, https://doi.org/10.1038/s41467-018-07954-9.

Dee, D. P., and Coauthors, 2011: The ERA-Interim reanalysis: Configuration and performance of the data assimilation system. *Quart. J. Roy. Meteor. Soc.*, **137**, 553–597, https://doi.org/10.1002/qj.828.

Deser, C., R. Tomas, M. Alexander, and D. Lawrence, 2010: The seasonal atmospheric response to projected Arctic sea ice loss in the late twenty-first century. *J. Climate*, **23**, 333–351, https://doi.org/10.1175/2009JCLI3053.1.

Ding, Q., J. M. Wallace, D. S. Battisti, E. J. Steig, A. J. E. Gallant, H.-J. Kim, and L. Geng, 2014: Tropical forcing of the recent rapid Arctic warming in northeastern Canada and Greenland. *Nature*, **509**, 209–212, https://doi.org/10.1038/nature13260.

ECMWF, 2014: IFS Documentation CY40R1–Part III: Dynamics and numerical procedures. ECMWF, 29 pp., https://www.ecmwf.int/en/elibrary/9203-ifs-documentation-cy40r1-part-iii-dynamics-and-numerical-procedures.

Feldstein, S. B., 2000: The timescale, power spectra, and climate noise properties of teleconnection patterns. *J. Climate*, **13**, 4430–4440, https://doi.org/10.1175/1520-0442(2000)013<4430:TTPSAC>2.0.CO;2.

——, 2002: The recent trend and variance increase of the annular mode. *J. Climate*, **15**, 88–94, https://doi.org/10.1175/1520-0442(2002)015<0088:TRTAVI>2.0.CO;2.

——, and S. Lee, 2014: Intraseasonal and interdecadal jet shifts in the Northern Hemisphere: The role of warm pool tropical convection and sea ice. *J. Climate*, **27**, 6497–6518, https://doi.org/10.1175/JCLI-D-14-00057.1.

Francis, J. A., and E. Hunter, 2006: New insight into the disappearing Arctic sea ice. *Eos, Trans. Amer. Geophys. Union*, **87**, 509–511, https://doi.org/10.1029/2006EO460001.

——, and ——, 2007: Changes in the fabric of the Arctic's greenhouse blanket. *Environ. Res. Lett.*, **2**, 045011, https://doi.org/10.1088/1748-9326/2/4/045011.

Franzke, C., 2009: Multi-scale analysis of teleconnection indices: Climate noise and nonlinear trend analysis. *Nonlin. Processes Geophys.*, **16**, 65–76, https://doi.org/10.5194/npg-16-65-2009

Fueglistaler, S., B. Legras, A. Beljaars, J. J. Morcrette, A. Simmons, A. M. Tompkins, and S. Uppala, 2009: The diabatic heat budget of the upper troposphere and lower/mid stratosphere in ECMWF reanalyses. *Quart. J. Roy. Meteor. Soc.*, **135**, 21–37, https://doi.org/10.1002/qj.361.

Gong, T., S. B. Feldstein, and S. Lee, 2017: The role of downward infrared radiation in the recent Arctic winter warming trend. *J. Climate*, **30**, 4937–4949, https://doi.org/10.1175/JCLI-D-16-0180.1.

Graversen, R. G., 2006: Do changes in the midlatitude circulation have any impact on the Arctic surface air temperature trend? *J. Climate*, **19**, 5422–5438, https://doi.org/10.1175/JCLI3906.1.

——, T. Mauritsen, M. Tjernström, E. Källén, and G. Svensson, 2008: Vertical structure of recent Arctic warming. *Nature*, **451**, 53–56, https://doi.org/10.1038/nature06502.

Hewitson, B. C., and R. G. Crane, 2002: Self-organizing maps: Applications to synoptic climatology. *Climate Res.*, **22**, 13–26, https://doi.org/10.3354/cr022013.

Hwang, Y.-T., and D. M. W. Frierson, 2010: Increasing atmospheric poleward energy transport with global warming. *Geophys. Res. Lett.*, **37**, L24807, https://doi.org/10.1029/2010GL045440.

Iacono, M. J., J. S. Delamere, E. J. Mlawer, M. W. Shephard, S. A. Clough, and W. D. Collins, 2008: Radiative forcing by long-lived greenhouse gases: Calculations with the AER radiative transfer models. *J. Geophys. Res.*, **113**, D13103, https://doi.org/10.1029/2008JD009944.

Johnson, N. C., and S. B. Feldstein, 2010: The continuum of North Pacific sea level pressure patterns: Intraseasonal, interannual, and interdecadal variability. *J. Climate*, **23**, 851–867, https://doi.org/10.1175/2009JCLI3099.1.

——, ——, and B. Tremblay, 2008: The continuum of Northern Hemisphere teleconnection patterns and a description of the NAO shift with the use of self-organizing maps. *J. Climate*, **21**, 6354–6371, https://doi.org/10.1175/2008JCLI2380.1.

Kohonen, T., 2001: *Self-Organizing Maps*. Springer, 501 pp., https://doi.org/10.1007/978-3-642-56927-2.

Kutzbach, J. E., 1967: Empirical eigenvectors of sea-level pressure, surface temperature and precipitation complexes over North America. *J. Appl. Meteor.*, **6**, 791–802, https://doi.org/10.1175/1520-0450(1967)006<0791:EEOSLP>2.0.CO;2.

Lee, S., and S. B. Feldstein, 2013: Detecting ozone- and greenhouse gas–driven wind trends with observational data. *Science*, **339**, 563–567, https://doi.org/10.1126/science.1225154.

——, T. Gong, N. C. Johnson, S. B. Feldstein, and D. Pollard, 2011: On the possible link between tropical convection and the Northern Hemisphere Arctic surface air temperature change between 1958 and 2001. *J. Climate*, **24**, 4350–4367, https://doi.org/10.1175/2011JCLI4003.1.

——, ——, S. B. Feldstein, J. Screen, and I. Simmonds, 2017: Revisiting the cause of the 1989–2009 Arctic surface warming using the surface energy budget: Downward infrared radiation dominates the surface fluxes. *Geophys. Res. Lett.*, **44**, 10 654–10 661, https://doi.org/10.1002/2017GL075375.

Lesins, G., T. J. Duck, and J. R. Drummond, 2012: Surface energy balance framework for Arctic amplification of climate change. *J. Climate*, **25**, 8277–8288, https://doi.org/10.1175/JCLI-D-11-00711.1.

Lu, J., and M. Cai, 2009: Seasonality of polar surface warming amplification in climate simulations. *Geophys. Res. Lett.*, **36**, L16704, https://doi.org/10.1029/2009GL040133.

Madden, R. A., 1976: Estimates of the natural variability of time-averaged sea-level pressure. *Mon. Wea. Rev.*, **104**, 942–952, https://doi.org/10.1175/1520-0493(1976)104<0942:EOTNVO>2.0.CO;2.

—— and D. J. Shea, 1978: Estimates of the natural variability of time-averaged temperatures over the United States. *Mon. Wea. Rev.*, **106**, 1695–1703, https://doi.org/10.1175/1520-0493(1978)106<1695:EOTNVO>2.0.CO;2.

Mlawer, E. J., S. J. Taubman, P. D. Brown, M. J. Iacono, and S. A. Clough, 1997: Radiative transfer for inhomogeneous atmospheres: RRTM, a validated correlated-*k* model for the longwave. *J. Geophys. Res.*, **102**, 16 663–16 682, https://doi.org/10.1029/97JD00237.

Prenni, A. J., and Coauthors, 2007: Can ice-nucleating aerosols affect Arctic seasonal climate? *Bull. Amer. Meteor. Soc.*, **88**, 541–550, https://doi.org/10.1175/BAMS-88-4-541.

Quinn, P. K., and Coauthors, 2008: Short-lived pollutants in the Arctic: Their climate impact and possible mitigation strategies. *Atmos. Chem. Phys.*, **8**, 1723–1735, https://doi.org/10.5194/acp-8-1723-2008.

Screen, J. A., and I. Simmonds, 2010: The central role of diminishing sea ice in recent Arctic temperature amplification. *Nature*, **464**, 1334–1337, https://doi.org/10.1038/nature09051.

——, C. Deser, and I. Simmonds, 2012: Local and remote controls on observed Arctic warming. *Geophys. Res. Lett.*, **39**, L10709, https://doi.org/10.1029/2012GL051598.

Sellers, W. D., 1969: A global climate model based on the energy balance of the Earth–atmosphere system. *J. Appl. Meteor.*, **8**, 392–400, https://doi.org/10.1175/1520-0450(1969)008<0392:AGCMBO>2.0.CO;2.

Seo, K. H., H. J. Lee, and D. M. Frierson, 2016: Unraveling the teleconnection mechanisms that induce wintertime temperature anomalies over the Northern Hemisphere continents in response to the MJO. *J. Atmos. Sci.*, **73**, 3557–3571, https://doi.org/10.1175/JAS-D-16-0036.1.

Serreze, M. C., and J. A. Francis, 2006: The Arctic amplification debate. *Climatic Change*, **76**, 241–264, https://doi.org/10.1007/s10584-005-9017-y.

——, A. P. Barrett, J. C. Stroeve, D. N. Kindig, and M. M. Holland, 2009: The emergence of surface-based Arctic amplification. *Cryosphere*, **3**, 11–19, https://doi.org/10.5194/tc-3-11-2009.

Sorokina, S. A., C. Li, J. J. Wettstein, and N. G. Kvamstø, 2016: Observed atmospheric coupling between Barents Sea ice and the warm-Arctic cold-Siberian anomaly pattern. *J. Climate*, **29**, 495–511, https://doi.org/10.1175/JCLI-D-15-0046.1.

Walsh, J. E., 2014: Intensified warming of the Arctic: Causes and impacts on middle latitudes. *Global Planet. Change*, **117**, 52–63, https://doi.org/10.1016/j.gloplacha.2014.03.003.

Woods, C., and R. Caballero, 2016: The role of moist intrusions in winter Arctic warming and sea ice decline. *J. Climate*, **29**, 4473–4485, https://doi.org/10.1175/JCLI-D-15-0773.1.

——, ——, and G. Svensson, 2013: Large-scale circulation associated with moisture intrusions into the Arctic during winter. *Geophys. Res. Lett.*, **40**, 4717–4721, https://doi.org/10.1002/grl.50912.

Yoo, C., S. B. Feldstein, and S. Lee, 2013: The prominence of a tropical convective signal in the wintertime Arctic temperature. *Atmos. Sci. Lett.*, **15**, 7–12, https://doi.org/10.1002/asl2.455.

Yuan, J., B. Tan, S. B. Feldstein, and S. Lee, 2015: Wintertime North Pacific teleconnection patterns: Seasonal and interannual variability. *J. Climate*, **28**, 8247–8263, https://doi.org/10.1175/JCLI-D-14-00749.1.